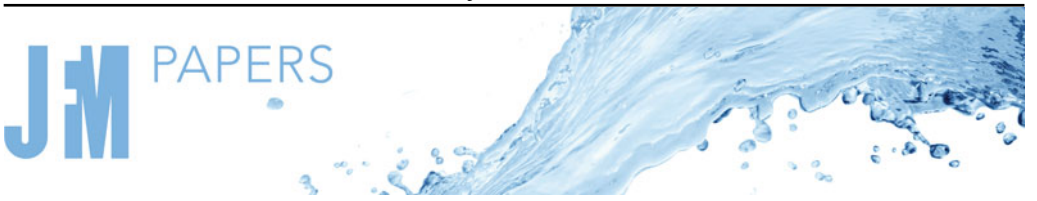
J. Fluid Mech. (2025), *vol.* 1020, A48, doi:10.1017/jfm.2025.10548



Wave and vortex structures in transitional mixing layers: a numerical investigation

Junlin Chen[1], **Xianyang Jiang**[1,2] **and Zuoli Xiao**[1,3]

[1]State Key Laboratory for Turbulence and Complex Systems, School of Mechanics and Engineering Science, Peking University, Beijing 100871, PR China

[2]Department of Applied Mathematics and Theoretical Physics, Centre for Mathematical Sciences, University of Cambridge, Cambridge CB3 0WA, UK

[3]HEDPS and Center for Applied Physics and Technology, School of Mechanics and Engineering Science, Peking University, Beijing 100871, PR China

Corresponding author: Zuoli Xiao, z.xiao@pku.edu.cn

(Received 26 May 2024; revised 6 July 2025; accepted 2 August 2025)

Laminar–turbulent transition in shear flow is complicated and follows many possible routes. In this study, we seek to examine a scenario based on three-dimensional (3-D) waves (Jiang *et al.,* 2020*, J. Fluid Mech.,* vol. 890, A11) in compressible mixing layers, and elucidate the role of 3-D waves in generating streamwise vorticity. The Eulerian–Lagrangian coupled method is used to track the evolution of flow structures. Qualitative evidence shows that localised 3-D waves travel coherently with vortex structures at the early transition stage, which is consistent with the behaviours of 3-D waves in boundary layer transitions. To examine the local flow events surrounding 3-D waves and investigate the cause and effect relationships inherent in wave–vortex interaction, the finite-time Lyapunov exponent and components of the strain rate tensor are integrated into evolving Lagrangian material surfaces. The formation of high-shear layers in the flanks of the 3-D waves is observed, driven by fluid ejection and sweep motions induced by the amplification of 3-D waves. The Λ-shaped vortices are found born in the vicinity of high-shear regions and then stretched into hairpin-shaped vortices farther downstream. Statistical findings reveal that streamwise vorticity develops concurrently with the significant growth of the oblique mode, while the normal motion of wave structures induces a high strain rate layer in the surrounding region. In addition, conditional statistics underscore the significance of high shear in enstrophy generation. Finally, a conceptual model is proposed to depict the evolution of coherent structures based on the relationship among the 3-D waves, high-shear/strain layers, and Λ-vortices, providing insights into their collective dynamics within transitional mixing layers.

Key words: transition to turbulence, shear layer turbulence, wave-turbulence interactions

© The Author(s), 2025. Published by Cambridge University Press.

https://doi.org/10.1017/jfm.2025.10548 Published online by Cambridge University Press

1. Introduction

The research on laminar–turbulent transition remains a challenging aspect of fluid mechanics, dating back to the pioneering work of Reynolds (1883). Generally, the transition of flow states initiates through a sequence of instabilities in a succession of increasingly complex basic flows, as described in Landau & Lifshitz (2013). With the advancements in flow visualisation and high-resolution numerical simulation techniques, detailed observations on the morphology and dynamics of flow structures have become a reality. Numerous structure-based transition and turbulence-sustaining models have been proposed and are continuously being developed (see e.g. Perry & Chong 1982; Smith *et al.* 1991; Waleffe 1997; Zhou *et al.* 1999; McKeon 2017; Jiménez 2018). However, it remains inconclusive which structure plays a pivotal role in the onset of turbulence.

For a considerable period, the hairpin vortex (represented by Λ- or Ω-shaped vortices in various topological forms, occurring at different stages of transition or during turbulent recycling) has been regarded as the fundamental coherent structure in both transitional and turbulent flows. Numerous studies have provided a comprehensive kinematic understanding of its configuration, including its shapes and scaling properties (see Head & Bandyopadhyay 1981; Perry & Marusic 1995; Townsend 1999; Adrian 2007; Wu & Moin 2009). Conceptual models have also been proposed to elucidate the relationship between hairpin vortices and other coherent structures. For instance, Smith *et al.* (1991) and Robinson (1991) individually proposed a model accounting for the regeneration of hairpin vortices. However, the onset of primary hairpins remains unclear. Besides the issue of origin, other dynamical characteristics of the hairpin vortex, such as cause and effect relationships, are poorly understood. This challenge arises from the difficulty of effectively tracking a complex vortex within an equally complex environment, as emphasised by Smith *et al.* (1991). Moin, Leonard & Kim (1986) investigated the phenomenology of Λ- and hairpin-vortex formation through Lagrangian (Biot–Savart) calculations, highlighting the influence of mean shear, though the role of perturbations received comparatively less emphasis.

In the realm of vortex formation dynamics in wall-bounded flows, Haidari & Smith (1994) conducted a study on the growth of a single hairpin vortex generated through the controlled injection of fluid from a streamwise slot beneath the wall. This heuristic experiment underscores the significance of three-dimensional (3-D) perturbations in the early transition phase, as the locally decelerated region created by the injection process is accompanied by an inflectional velocity profile. A similar mechanism occurs in natural transition, resulting from the mode resonance of disturbance waves. For instance, Benney (1961) introduced the concept of 'direct resonance' for shear flow instability, and Jang, Benney & Gran (1986) applied this concept to the interpretation of streamwise vortex formation. A parallel transition scenario is evidenced in a series of experimental works (Lee 1998, 2000) where the local 3-D perturbation was initially treated as a coherent structure named a soliton-like coherent structure, which was found to trigger the formation of a high shear layer through interaction with the mean shear, ultimately giving rise to the appearance of hairpin structures. These 'wave-like' structures can be traced back to experiments by Hama, Long & Hegarty (1957), who identified a special kink structure preceding hairpin vortex formation, and concluded that the kink might serve as the origin of hairpin vortices. Jiang *et al.* (2020*a*,*b*) validated the existence of these 3-D wave structures and their contribution to formation of vortex structures by using the Lagrangian particle tracking techniques based on velocity fields obtained from tomographic particle image velocimetry measurements. In this context, the recently discovered 3-D wave with soliton-like properties could assume a more foundational role in transitional and turbulent

https://doi.org/10.1017/jfm.2025.10548 Published online by Cambridge University Press

shear flows. Nonetheless, there is a need for a quantitative relationship between the amplification of disturbance waves and the formation of hairpin vortices.

In the absence of wall confinement, does the constitutive structure of the mixing layer resemble that of the boundary layer? This paper delves into the origin and development of hairpin vortices in the transitional region of mixing layers. It is widely acknowledged that a mixing layer transition initiates from Kelvin–Helmholtz instability or, in terms of 'structure' language, the corresponding Kelvin–Helmholtz waves. In the presence of 3-D perturbations, the two-dimensional (2-D) waves undergo secondary instability and later evolve into quasi-streamwise vortices. These secondary vortices are often observed in the form of ribs between two neighbouring Kelvin–Helmholtz rollers. For example, Konrad (1976) clearly visualised periodic streamwise streaks, with their spanwise spacing increasing downstream in proportion to the mixing layer thickness. Previous research works also manifest that 3-D waves are important in the development of compressible mixing layer at high convective Mach numbers. Chen, Cantwell & Mansour (1989) investigated the nonlinear mechanism for formation of characteristic structures in compressible free shear flows from the Eulerian perspective, and made a 3-D topological description of the flow by applying a generalised critical point method. It is found that streamwise vorticity in the saddle point regions is stretched by the strain field that results from the spanwise rollers. Meanwhile, Sandham (1989) suggested that the formation of four regions of strong rotation staggered in the streamwise direction should be attributed to the influence of oblique 3-D waves. At higher convective Mach numbers, these local structures of strong rotation are found to be pairs of hairpin-like vortical structures. In addition, Sandham & Reynolds (1991) reported that the oblique modes become increasingly dominant once the convective Mach number exceeds 0.6, which is a milestone for the investigation on instability structures and development of a compressible mixing layer.

By conducting high-resolution simulations of a compressible mixing layer at convective Mach number 0.7, Zhou, He & Shen (2012) obtained the temporal–spatial evolution of coherent structures throughout the entire transition process. The identified structures include Λ-vortices, hairpin vortices and 'flower' structures, which were also reported in simulations of boundary layer flows (Rist & Fasel 1995). Recently, Jiang *et al.* (2022) reported an investigation on the origin of Λ-vortices in a stratified mixing layer, which reveals that the wave-induced scenario of the vortex mirrors the dynamic process of boundary layer transition. The dynamics of these structures in transitional mixing layer flows, however, remains incompletely understood, particularly regarding the cause and effect relationships involved in structure interactions. Specifically, our understanding of the origin of streamwise vortices and the causal laws governing the structural evolution has been limited.

The rest of the paper is organised as follows. First, numerical methods for direct numerical simulations (DNS) and analysis approaches are introduced in § 2. Next, basic features of transition are described qualitatively in §§ 3.1 and 3.2, including the co-evolution of wave/vortex structures and the corresponding evidence, which suggests that 3-D waves trigger streamwise vortical structures. Then the cause and effect mechanism is elucidated by visualising shear layer deformation in § 3.3. After that, quantitative statistics are obtained to analyse structure dynamics in § 4. Specifically, the energy developments of different modes are compared in § 4.1, while the formation of streamwise vorticity and the role played by the local high strain rate in this process are examined in §§ 4.2 and 4.3, respectively. The effects of high convective Mach number are briefly analysed in § 4.4. Section 5 makes a comparison between the scenarios of mixing layer and boundary layer

https://doi.org/10.1017/jfm.2025.10548 Published online by Cambridge University Press

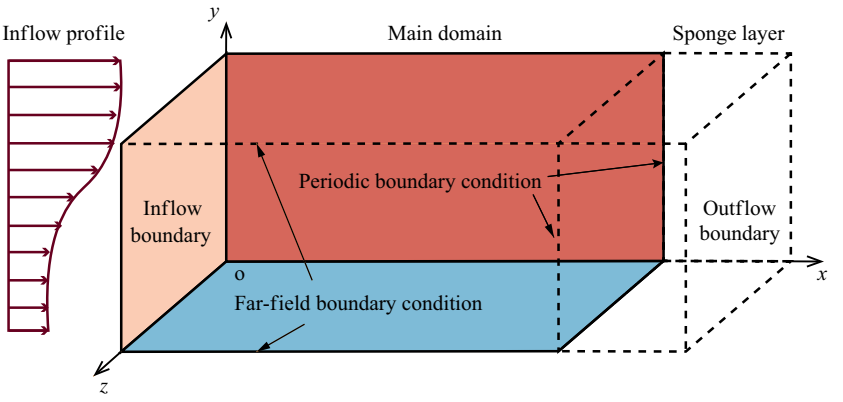


Figure 1. Schematic of the computational domain, boundary conditions and basic laminar flow.

	Parameters			Disturbance				
	M_c	Re	Modes	Variables	ω_0	β_0	a_0	a_1
CaseA	0.7	10 000	$(1,0),(0.5,\pm1)$	u, v, w	0.41	0.36	0.1	0.01
CaseA–F	0.7	10 000	$(1,0),(0.5,\pm1)$	u, v, w	0.41	0.36	0.1	0.01
CaseA–S	0.7	10 000	$(1,0),(0.5,\pm1)$	u, v, w	0.12	0.36	0.1	0.01
CaseB	1.4	10 000	$(1,0),(0.5,\pm1)$	u, v, w	0.18	0.51	0.1	0.1
Case1	0.7	800	$(1,0),(0.5,\pm1)$	v	0.41	0.36	1.0	0.2
Case2	0.7	800	$(1,0),(1,\pm1)$	u, v, w	0.41	0.36	1.0	0.2
Case3	0.7	800	$(1,\pm1)$	ρ, u, v, w, p	0.41	0.36	0.2	0.2
Case4	0.7	800	SDFM	u, v, w	–	–	–	–
Case5	1.4	1500	$(1,0),(0.5,\pm1)$	v	0.18	0.51	1.0	0.2
Zhou *et al.* (2012)	0.7	800	$(1,0),(0.5,\pm1)$ + VD	u, v, w	0.41	0.36	0.2	0.2

Table 1. Numerical settings for present simulations. The disturbance is in the form $u_i' = \mathrm{Re}[a_0\,\phi_0(y)\,e^{-i\omega_0} + a_1\,\phi_1^+(y)\,\mathrm{e}^{\mathrm{i}(\beta_0 z-\omega_1 t)} + a_1\,\phi_1^-(y)\,\mathrm{e}^{\mathrm{i}(-\beta_0 z-\omega_1 t)}]$. A normalised notation $(\omega/\omega_0, \beta/\beta_0)$ is used for mode description. The first digit indicates multiples of the fundamental streamwise frequency ω_0 , and the second digit refers to multiples of the fundamental spanwise wavenumber β_0. Here, 'SDFM' means the synthetic digital filtering method (Klein, Sadiki & Janicka 2003), and 'VD' denotes vortical disturbance.

flows, along with the interpretation of wave dynamics. Finally, concluding remarks are given in § 6.

2. Methodology

2.1. *Computation details*

A spatially developing compressible mixing layer is studied through DNS. The configuration of the mixing layer is illustrated in figure 1. Nine simulation cases are considered, with different parameters and types of disturbance, as detailed in table 1. The mixing layer, initially in a laminar state, is characterised by a thin layer between two free streams with distinct streamwise velocities but uniform density and pressure. In this study, the laminar properties of the mixing layer are employed to define a non-dimensionalised system. Laminar density, streamwise velocity, temperature and viscosity for the upper high-speed and lower low-speed streams are denoted as ρ_1^*, U_1^*, T_1^*, μ_1^* and ρ_2^*, U_2^*, T_2^*, μ_2^*, respectively. The quantities of the upper stream, e.g. ρ_1^*, serve as

https://doi.org/10.1017/jfm.2025.10548 Published online by Cambridge University Press

reference scalings. The length scale is defined as $\delta^*_\omega = \Delta U^*/|\mathrm{d}\bar{u}^*/\mathrm{d}y|_{max}$, referred to as the 'vorticity thickness' of the mixing layer, where ΔU^* represents the velocity difference between the high- and low-speed layers, while $\mathrm{d}\bar{u}^*/\mathrm{d}y$ denotes the derivative of initial streamwise velocity in the normal direction. Consequently, the Reynolds number and Mach number are defined as $Re = \rho^*_1 U^*_1 \delta^*_\omega/\mu^*_1$ and $Ma = U^*_1/\sqrt{\gamma R T^*_1}$, where $\gamma = 1.4$ represents the heat capacity ratio, and $R = 8.314$ J K^{-1} mol^{-1} is the universal gas constant.

In this study, we continue to use the computational domain specified by Zhou *et al.* (2012), which is defined as $[0, 54L_x] \times [-L_y/2, L_y/2] \times [0, 2L_z]$, where $L_x = 2\pi/\alpha$, $L_y = 400$ and $L_z = 2\pi/\beta$, with $\alpha = 0.54$ and $\beta = 0.36$ representing the most unstable wavenumbers from linear stability theory (LST). The domain is bounded by inflow and outflow boundaries in the streamwise (x) direction, two non-reflecting boundaries in the normal (y) direction, and two periodic boundaries in the spanwise (z) direction. The dimensionless velocities of upper stream U_1 and lower stream U_2 are set to 1.0 and 0.5, respectively. The Reynolds number and the reference Mach number are specified as 800 and 2.8, respectively, for low-Mach cases (Case1–Case4). Those two parameters are 1500 and 5.6, respectively, for the high-Mach case (Case5). For CaseA and CaseB, the Reynolds number is set to 10 000 to validate the growth rate of unstable waves by by comparing it with the corresponding mode amplification rates calculated from LST. Assuming equal specific heats and temperatures yields a convective Mach number $M_c = (Ma_1 - Ma_2)/2 = 0.7$ or 1.4. The pressures of both free streams are identical to each other and equal to $1/(\gamma\, Ma_1^2)$. At the inflow boundary, the unperturbed basic inflow profile of the streamwise velocity is obtained by solving compressible boundary layer equations. In addition, the inflow is forced by 3-D unstable waves. Readers are encouraged to consult Appendix A for more detailed description of how the disturbances are imposed.

The non-dimensionalised compressible Navier–Stokes equations are solved numerically using a finite difference solver on non-staggered grids, which read

$$\frac{\partial \rho}{\partial t} + \nabla \cdot (\rho \boldsymbol{u}) = 0, \tag{2.1}$$

$$\frac{\partial \rho \boldsymbol{u}}{\partial t} + \nabla \cdot (\rho \boldsymbol{u}\boldsymbol{u} - \boldsymbol{\tau}) = 0, \tag{2.2}$$

$$\frac{\partial \rho E}{\partial t} + \nabla \cdot (\rho E \boldsymbol{u} - \boldsymbol{\tau}\boldsymbol{u}) = \boldsymbol{q}. \tag{2.3}$$

Here, ρ, $\boldsymbol{u} = (u, v, w)$ and $E = C_V T + 1/2|\boldsymbol{u}|^2$ represent the fluid density, velocity and total energy per unit mass, respectively. The specific heat capacity at constant volume C_V is expressed as $1/\gamma(\gamma - 1)\, Ma_1^2$. The shear stress tensor and heat flux are denoted by $\boldsymbol{\tau} = \tau_{ij}$ and $\boldsymbol{q} = q_i$, respectively, and take the forms

$$\tau_{ij} = -p\, \delta_{ij} + \frac{2\mu}{Re}\left(S_{ij} - \frac{1}{3}\nabla \cdot \boldsymbol{u}\, \delta_{ij}\right) \tag{2.4}$$

and

$$q_i = -\frac{\mu}{(\gamma - 1)\, Ma_1^2\, Re\, Pr}\frac{\partial T}{\partial x_i}. \tag{2.5}$$

Here, p is pressure, T is temperature, and $\boldsymbol{S} = S_{ij} = 1/2(\partial u_i/\partial x_j + \partial u_j/\partial x_i)$ is the strain rate tensor. The dynamic viscosity μ is evaluated using Sutherland's law, and $Pr = 0.7$

https://doi.org/10.1017/jfm.2025.10548 Published online by Cambridge University Press

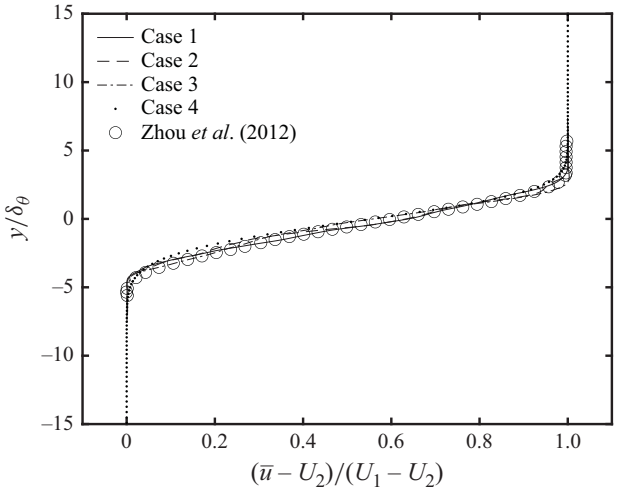


Figure 2. Profiles of the mean streamwise velocity $\bar{u}$ across mixing layers within the fully developed turbulent region for different cases. The numerical data from Zhou *et al.* (2012) are included for comparison.

denotes the Prandtl number. The above equations are complemented by the perfect gas law $p = \rho T/\gamma Ma_1^2$.

The nonlinear terms in (2.2) are discretised using a hybrid seventh-order linear scheme, a seventh-order weighted essentially non-oscillatory (WENO) scheme, and a fifth-order WENO scheme (Shu 1998). The viscous terms are discretised using an eighth-order-accurate central difference scheme. Temporal advancement of the equations is achieved using a third-order total variation diminishing Runge–Kutta multistage method. In Case1, for example, the grid numbers are 4160, 350 and 256 along the x-, y- and z-directions, respectively. In the x-direction, the first 4000 grid points are uniformly spaced from $x = 0$ to $x = 50L_x$, while the remaining 160 grid points are stretched from $x = 50L_x$ to $x = 54L_x$ to create a buffer range. In the normal direction, to capture fine structures in the mixing layer, the grid is concentrated in the middle zone and stretched to the far-field boundaries. Approximately 46 grid points are distributed within the early-stage centre layer around the inflow region, which remains predominantly laminar, while approximately 115 grid points are allocated within the downstream centre layer close to the outflow region, which reaches the fully turbulent state (the corresponding results are not shown here). The numerical settings are validated by comparing the averaged streamwise velocity profile in the fully developed turbulent region with that reported by Zhou *et al.* (2012), as shown in figure 2. The computations are accelerated by Nvidia V100 GPU cards.

2.2. *Linear stability analysis*

It is essential to validate whether the numerical code is efficient for flows involving both shockwaves and growth of instabilities (Sandham & Yee 1989). To this end, the value of the imaginary part of the most unstable streamwise wavenumber $\alpha_{0,i}$ needs to be compared with the growth rate of mode energy calculated by DNS as suggested by Kim, Moin & Moser (1987). The detailed derivation of LST equations follows Sandham (1989).

https://doi.org/10.1017/jfm.2025.10548 Published online by Cambridge University Press

One can start with the Eulerian equations in the form

$$\frac{\partial \rho}{\partial t} + u_i \frac{\partial \rho}{\partial x_i} + \rho \frac{\partial u_i}{\partial x_i} = 0, \tag{2.6a}$$

$$\rho \left(\frac{\partial u_i}{\partial t} + u_j \frac{\partial u_i}{\partial x_j} \right) = -\frac{1}{\gamma M_1^2} \frac{\partial p}{\partial x_i}, \tag{2.6b}$$

$$\rho \left(\frac{\partial T}{\partial t} + u_i \frac{\partial T}{\partial x_i} \right) = -p(\gamma - 1) \frac{\partial u_i}{\partial x_i}, \tag{2.6c}$$

$$p = \rho T. \tag{2.6d}$$

Decomposing the flow variables into a basic flow part and a disturbance part, and assuming travelling wave solutions for the latter, i.e.

$$u = \bar{u} + u', \quad v = v', \quad w = w', \quad T = \bar{T} + T', \quad \rho = \bar{\rho} + \rho', \quad p = 1 + p', \tag{2.7}$$

$$\left(u', v', w', T', \rho', p'\right) = (\hat{u}, \hat{v}, \hat{w}, \hat{T}, \hat{\rho}, \hat{p})\, \mathrm{e}^{\mathrm{i}(\alpha x + \beta z - \omega t)}, \tag{2.8}$$

one can readily obtain the linearised disturbance equations

$$\hat{\rho} i(\alpha \bar{u} - \omega) + \hat{v}\, \mathrm{D}\bar{\rho} + \bar{\rho}[i(\alpha \hat{u} + \beta \hat{w}) + \mathrm{D}\hat{v}] = 0, \tag{2.9a}$$

$$\bar{\rho}[i(\alpha \bar{u} - \omega)\hat{u} + \hat{v}\, \mathrm{D}\bar{u}] = \frac{-i\alpha \hat{p}}{\gamma M_1^2}, \tag{2.9b}$$

$$\bar{\rho} i(\alpha \bar{u} - \omega)\hat{v} = \frac{-\mathrm{D}\hat{p}}{\gamma M_1^2}, \tag{2.9c}$$

$$\bar{\rho} i(\alpha \bar{u} - \omega)\hat{w} = \frac{-i\beta \hat{p}}{\gamma M_1^2}, \tag{2.9d}$$

$$\bar{\rho}[i(\alpha \bar{u} - \omega)\hat{T} + \hat{v}\, \mathrm{D}\bar{T}] = -(\gamma - 1)[i(\alpha \hat{u} + \beta \hat{w}) + \mathrm{D}\hat{v}], \tag{2.9e}$$

$$\hat{p} = \bar{\rho}\hat{T} + \hat{\rho}\bar{T}, \tag{2.9f}$$

with $\mathrm{D} \equiv \mathrm{d}/\mathrm{d}y$ denoting the derivative operator with respect to y. For a spatially developing mixing layer, the disturbance equations can be written as a linear system $A_s \boldsymbol{x} = \alpha B_s \boldsymbol{x}$, where $\boldsymbol{x} = (\hat{\rho}, \hat{u}, \hat{v}, \hat{w}, \hat{T})^{\mathrm{T}}$:

$$A_s = \begin{pmatrix} \omega & 0 & i(\mathrm{D}\bar{\rho} + \bar{\rho}\,\mathrm{D}) & -\beta\bar{\rho} & 0 \\ 0 & \omega & i\,\mathrm{D}\bar{u} & 0 & 0 \\ \frac{i(\mathrm{D}\bar{T} + \bar{T}\,\mathrm{D})}{\bar{\rho}\gamma M_1^2} & 0 & \omega & 0 & \frac{i(\mathrm{D}\bar{\rho} + \bar{\rho}\,\mathrm{D})}{\bar{\rho}\gamma M_1^2} \\ \frac{-i\beta\bar{T}}{\bar{\rho}\gamma M_1^2} & 0 & 0 & \omega & \frac{-\beta}{\gamma M_1^2} \\ 0 & 0 & i\left(\mathrm{D}\bar{T} + \frac{(\gamma-1)\,\mathrm{D}}{\bar{\rho}}\right) & \frac{-(\gamma-1)\beta}{\bar{\rho}} & \omega \end{pmatrix} \tag{2.10}$$

https://doi.org/10.1017/jfm.2025.10548 Published online by Cambridge University Press

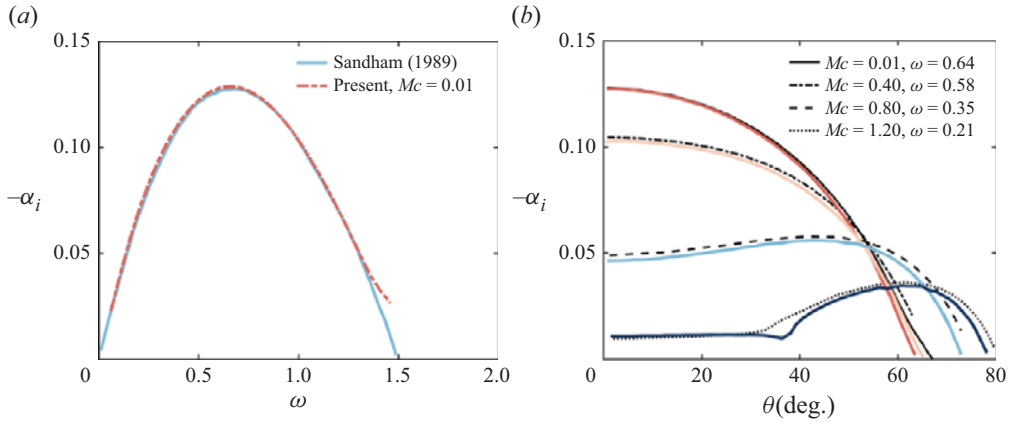


Figure 3. (*a*) Spatial amplification rate of the mixing layer ($-\alpha_i$) against frequency ω at $Mc = 0.01$. (*b*) Spatial amplification rate of the mixing layer ($-\alpha_i$) against the angle of oblique waves θ for different convective Mach numbers and frequencies, which are calculated through linear stability analysis. In (*b*), the black lines denote present results, while solid coloured lines represent the calculations from Sandham (1989).

and

$$B_s = \begin{pmatrix} \bar{u} & \bar{\rho} & 0 & 0 & 0 \\ \frac{T}{\bar{\rho}} & \bar{u} & 0 & 0 & \frac{1}{\gamma M_1^2} \\ \bar{\rho} M_1^2 & 0 & \bar{u} & 0 & 0 \\ 0 & 0 & 0 & \bar{u} & 0 \\ 0 & \frac{\gamma-1}{\bar{\rho}} & 0 & 0 & \bar{u} \end{pmatrix}. \tag{2.11}$$

The second-order central difference scheme is employed to discretise the differential operators in matrix A_s of the disturbance equation system. Shown in figure 3(*a*,*b*) are the spatial amplification rate of the mixing layer ($-\alpha_i$) against frequency ω at $Mc = 0.01$, and that against the angle of oblique waves θ for different convective Mach numbers and frequencies, respectively, which are calculated through linear instability analysis. The correctness of present results and reliability of our code are validated in comparison with the corresponding results from Sandham (1989), who used the shooting method to solve the eigenvalue problem. Note that it is within expectation that the direct method loses some accuracy near the neutral mode. It is hard to capture weak amplified waves, especially at high Mach numbers. However, the direct method is faster than the shooting method, and meets the accuracy requirement near the most unstable mode. Furthermore, figure 4 provides a comparison between the imaginary part of the most unstable wavenumber $-\alpha_{0,i}$ from LST and (half) the growth rate of mode kinetic energy $E_k(\omega, \beta) = \int_{-L_y/2}^{L_y/2} \hat{u}_i \hat{u}_i^c \, \mathrm{d}y$ from DNS for two convective Mach numbers (0.7 and 1.4), which validates the effectiveness of the present numerical code.

To further validate the effectiveness of the present numerical code in capturing the subsonic and supersonic modes, both the LST and DNS results are obtained for the subsonic (fast) and supersonic (slow) modes of the test case with $Mc = 0.7$. Those two numerical simulations correspond to CaseA–F and CaseA–S as listed in table 1. The amplification rates of fast and slow modes given by LST are $-\alpha_i = 0.063$ and 0.013, respectively. As expected, the most amplified mode is the fast mode, in good consistency with the conclusion from either Sandham (1989) or Grosch & Jackson (1991). The corresponding amplification rates from DNS are also presented in figure 4, which turn out

https://doi.org/10.1017/jfm.2025.10548 Published online by Cambridge University Press

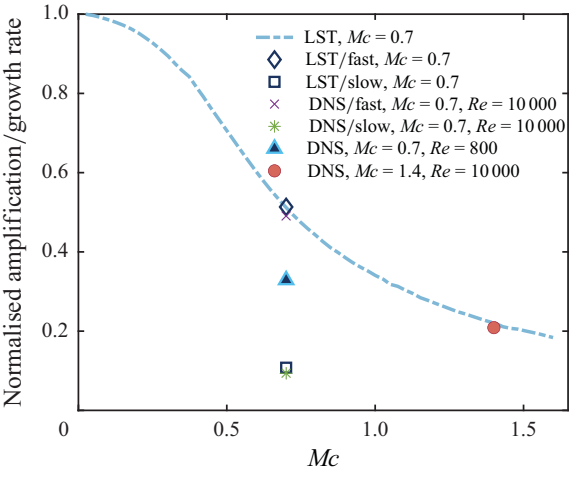


Figure 4. The spatial amplification rate of the most unstable wave ($\alpha_{0,i}$) from LST (dashed line) and half the growth rate of kinetic energy $E_k(\omega/\omega_0, \beta/\beta_0)$ in mode (1, 0) from DNS against the convective Mach number (Mc). The results of both subsonic (fast) and supersonic (slow) modes from LST and DNS are also provided for comparison in the test case $Mc = 0.7$. The amplification rate and growth rate are normalised by their incompressible counterparts, respectively.

to be in good alignment with LST. These calculations confirm the validity of the employed code in capturing the subsonic and supersonic modes.

2.3. *Measurement of deformation*

Building upon the data generated by DNS, a theoretical analysis is conducted to quantitatively investigate the mechanism of wave–vortex interaction. This analysis is rooted in the governing equation of vorticity ($\boldsymbol{\omega} = \boldsymbol{\nabla} \cdot \boldsymbol{u}$)

$$\begin{aligned}\frac{\partial \boldsymbol{\omega}}{\partial t} = &-(\boldsymbol{u}\cdot\boldsymbol{\nabla})\boldsymbol{\omega} - \boldsymbol{\omega}(\boldsymbol{\nabla}\cdot\boldsymbol{u}) + (\boldsymbol{\omega}\cdot\boldsymbol{\nabla})\boldsymbol{u} - \frac{1}{\rho^2}\boldsymbol{\nabla} p\cdot\boldsymbol{\nabla}\rho \\ &+ \frac{\mu}{Re}\left[\frac{1}{\rho}\nabla^2\boldsymbol{\omega} - \frac{1}{\rho^2}\boldsymbol{\nabla}\rho\cdot\left(\nabla^2\boldsymbol{u} + \frac{1}{3}\boldsymbol{\nabla}(\boldsymbol{\nabla}\cdot\boldsymbol{u})\right)\right].\end{aligned} \tag{2.12}$$

The terms on the right-hand side of (2.12) represent the contributions of convection, dilation, stretching/tilting, baroclinic effect and viscous dissipation, respectively. Vortex stretching and tilting lead to the creation of Λ-shaped and subsequent hairpin vortices. The production of enstrophy ($\boldsymbol{\omega}^2/2$, which measures the vortex intensity) by vortex stretch/tilting can be expressed as

$$\boldsymbol{\omega}\cdot\boldsymbol{\nabla}\boldsymbol{u}\cdot\boldsymbol{\omega} = \boldsymbol{\omega}^{\mathrm{T}}\boldsymbol{S}\boldsymbol{\omega}, \tag{2.13}$$

where $\boldsymbol{S} = (1/2)[\boldsymbol{\nabla}\boldsymbol{u} + (\boldsymbol{\nabla}\boldsymbol{u})^{\mathrm{T}}]$ is the strain rate tensor. To describe the geometry, orientation and dynamics of vortices, the analyis is usually carried out based on the eigenvalues and eigenvectors of strain rate tensor $\boldsymbol{S}$, as reported by Kida & Tanaka (1994) for homogeneous shear flows, and Bechlars & Sandberg (2017) for boundary layer flows. For example, the production term (2.13) can be further decomposed into

$$\boldsymbol{\omega}^{\mathrm{T}}\boldsymbol{S}\boldsymbol{\omega} = 2|\boldsymbol{A}|^2|\boldsymbol{S}|\sum_{i=1}^{3}\beta_i\cos^2(\langle\boldsymbol{\omega}, \boldsymbol{\Lambda}_i\rangle), \tag{2.14}$$

https://doi.org/10.1017/jfm.2025.10548 Published online by Cambridge University Press

where $\boldsymbol{A} = (1/2)[\nabla \boldsymbol{u} - (\nabla \boldsymbol{u})^{\mathrm{T}}]$ is the asymmetric part of the velocity gradient, and β_i $(i = 1, 2, 3)$ and $\boldsymbol{\Lambda}_i$ are the normalised eigenvalues and eigenvectors of the strain rate tensor, respectively. The angles between vorticity vector and eigenvectors are denoted by $\langle \boldsymbol{\omega}, \boldsymbol{\Lambda}_i \rangle$.

For the Lagrangian description of coherent structures, a set of timelines or the time sequence of a material surface can be used to visualise the evolving history of a parcel of fluids. To this end, a line or plane of particle tracers is released at a specific instant and position of the flow field, then tracked in time based on the Lagrangian method (Jiang *et al.* 2021). Given a velocity field $\boldsymbol{u}(\boldsymbol{x}, t)$, the path of each particle $\boldsymbol{X}(t)$ can be obtained by integrating the ordinary differential equation

$$\dot{\boldsymbol{X}} = \boldsymbol{u}(\boldsymbol{X}, t), \quad t \in [t_0, t_1], \tag{2.15}$$

with solution $\boldsymbol{X}(t; t_0, \boldsymbol{X}_0)$. Thus the Lagrangian description of fluid motion takes the form of a flow map $F_{t_0}^t$:

$$F_{t_0}^t(\boldsymbol{X}_0) = \boldsymbol{X}(t; t_0, \boldsymbol{X}_0), \quad t \in [t_0, t_1]. \tag{2.16}$$

As far as a hypersurface in a 3-D space is concerned, an evolving material line $\boldsymbol{L}$ or a material surfaces $\boldsymbol{M}$ initiated at time t_0 can be defined as

$$\boldsymbol{L}(t) := F_{t_0}^t(\boldsymbol{L}(t_0)) \tag{2.17}$$

and

$$\boldsymbol{M}(t) := F_{t_0}^t(\boldsymbol{M}(t_0)), \tag{2.18}$$

respectively. In this study, the timelines and material surfaces are released at positions within the mixing layer. The metamorphosis of the material elements can reveal the evolution of flow structures, a process that is challenging to discern within the Eulerian framework.

To quantitatively investigate the relationship between the deformation of material elements (lines or surfaces) and flow structures, we calculate the geometric characteristics of material entities. In continuum mechanics, the deformation of an object is typically represented by strain tensors, such as the Cauchy–Green tensor

$$C(\boldsymbol{X}_0) = [\nabla F_{t_0}^t(\boldsymbol{X}_0)]^{\mathrm{T}} \nabla F_{t_0}^t(\boldsymbol{X}_0). \tag{2.19}$$

The stretching of fluids in the Lagrangian framework can be determined through considering the eigencharacter of the Cauchy–Green tensor, such as the finite-time Lyapunov exponent (FTLE) and the alignment of eigenvectors. Specifically, the FTLE is introduced below for the purpose of visualising fluid stretching (Haller 2001). The FTLE represents the rate of separation of neighbouring particle trajectories initialised near that point:

$$\Lambda_{t_0}^{t_1}(\boldsymbol{X}_0) = \frac{1}{t_1 - t_0} \log \sqrt{\lambda_n(\boldsymbol{X}_0)}. \tag{2.20}$$

In this definition, the largest possible stretching at a point $\boldsymbol{X}_0$ is given by $\sqrt{\lambda_n(\boldsymbol{X}_0)}$, where λ_n is the largest eigenvalue of $C(\boldsymbol{X}_0)$, with $n = 3$ for 3-D flows. As a geometrical illustration, a material sphere with infinitesimally small radius r_0 initialised at t_0 is assumed to be transported by a 3-D flow (see figure 5). The sphere deforms into a small ellipsoid, which represents the change of local strain state $\boldsymbol{S}(x, t)$ in the flow field. The length of the ith principal axis of the sphere is $\sqrt{\lambda_i(X_0)}$ $(i = 1, 2, 3)$ multiplied by the radius of the initial sphere.

In practice, integrating trajectories forwards in time ($t_1 > t_0$) may produce FTLE ridges that mark the locations of repelling Lagrangian coherent structures. If the FTLE is

https://doi.org/10.1017/jfm.2025.10548 Published online by Cambridge University Press

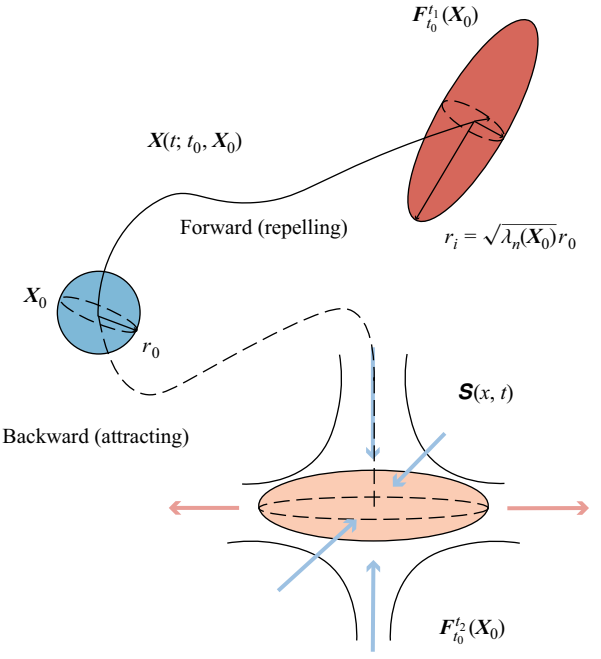


Figure 5. Schematics of the deformation of a fluid parcel. Two types of Lagrangian trajectories $F^t_{t_0}(\boldsymbol{X}_0)$ are illustrated. Forward tracking (solid line, $t_1 > t_0$) detects 'repelling' Lagrangian structures, while backward tracking (dashed line, $t_2 < t_0$) detects 'attracting' ones. The Lagrangian deformation, e.g. stretching (the light orange arrows) or compression (the light blue arrows), is the integral effects of local strain rate $\boldsymbol{S}(x, t)$.

calculated by integrating trajectories backwards in time ($t_2 < t_0$), then ridges in the FTLE field may indicate attracting material lines or attracting Lagrangian coherent structures. Examples of attaining 'attracting' structures through backward tracking can be found in the literature (see e.g. Green, Rowley & Haller 2007; Zhao, Yang & Chen 2016). Hairpin vortices are detected for temporally developing channel flows in these studies. In the present study, the forward tracking method is employed for the spatially evolving structures in all cases to avoid determining the positions of flow structures in advance.

3. Visualisation of flow structures

In this study, focus is placed on the investigation of both wave and vortex structures, aiming to quantify the coupling mechanism of these two types of structures in the early transition stage. Without loss of generality, the results for Case1 are selected in the subsequent discussion. The quantitative relationships provide insights, from the perspective of structural evolution, into the mechanism that leads to the transition from laminar to turbulent flow. We approach this classical problem using data-driven methods because it is challenging to deduce the mechanism of such nonlinear structural evolution analytically. The coupled Eulerian–Lagrangian method is employed to capture the coherent structures and trace their dynamic evolutions.

3.1. *Co-existence of wave and vortex structures*

We begin with the visualisation of the instantaneous flow field to offer an intuitive picture of the co-existing state of coherent structures in the mixing region. Furthermore, we will initiate the qualitative description of the wave–vortex relation, incorporating fundamental

https://doi.org/10.1017/jfm.2025.10548 Published online by Cambridge University Press

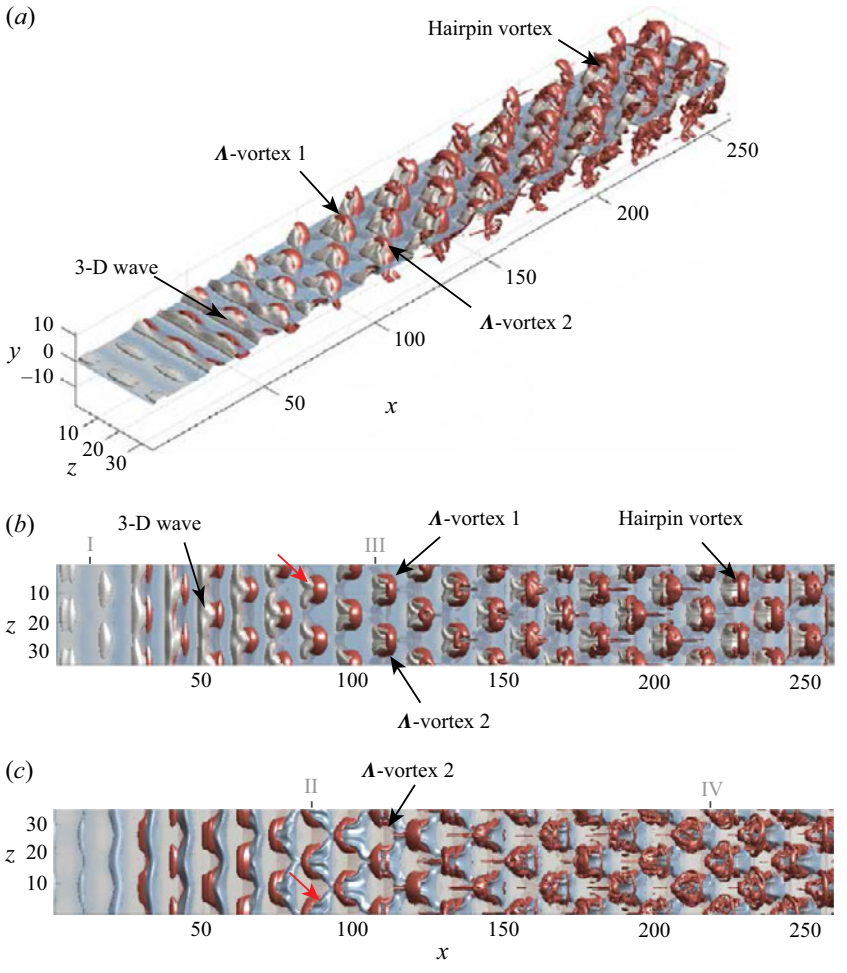


Figure 6. Spatial distribution of the perturbation waves and vortices in Case1. The wave structures are visualised by iso-surfaces of the conditioned normal velocity at the plane $y_c = 0.08$, which is located approximately at the mixing layer centre. The vortex structures are represented by iso-surfaces of the second invariant of velocity gradient tensor, i.e. $Q = 8 \times 10^{-3}$. (*a*) Oblique view of the 3-D flow structures. (*b*) Top-down view with the normal velocity positively conditioned. (*c*) Bottom-up view with the normal velocity negatively conditioned. The conditioned normal velocity fields in (*a*), (*b*) and (*c*) are magnified 30 times in scale.

flow events such as lift-up. The Taylor frozen hypothesis is employed to deduce the underlying dynamical process from the spatial evolution of flow structures.

Figure 6(*a*) is an oblique view of the 3-D flow structures, which display the growth and metamorphosis of both disturbance waves (represented by positive conditioned normal velocity field v) and vortical structures (identified by the second invariant of velocity gradient $Q = 1/4\omega_i\omega_i - 1/2S_{ij}S_{ij}$) from inlet to the downstream regions. The normal velocity under the positive condition is defined as

$$v_c^p(x, z) = \begin{cases} v(x, y_c, z) & \text{if } v > 0, \\ 0 & \text{if } v \leqslant 0, \end{cases} \tag{3.1}$$

https://doi.org/10.1017/jfm.2025.10548 Published online by Cambridge University Press

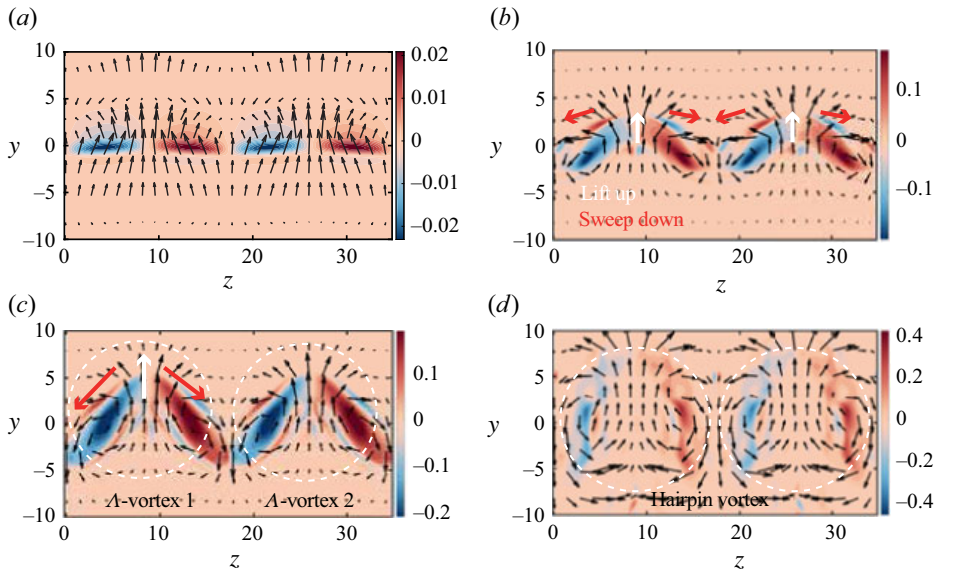


Figure 7. Evolution of streamwise vortical structures in z–y slices at a sequence of streamwise positions: (a) $x = 16$, (b) $x = 85$, (c) $x = 110$, and (d) $x = 227$, as shown in figure 6 labelled by I, II, III and IV, respectively. The contours are for the streamwise vorticity, while the vectors represent the combination of normal velocity v and spanwise velocity w.

in which y_c is the vertical coordinate of the mixing layer centreline. Similarly, the negatively conditioned normal velocity is defined as

$$v_c^n(x, z) = \begin{cases} v(x, y_c, z) & \text{if } v < 0, \\ 0 & \text{if } v \geqslant 0. \end{cases} \tag{3.2}$$

Figure 6(b,c) show respectively a top-down view and a bottom-up view of the flow structures in the same region as figure 6(a), where wave structures are again visualised by either a positively or negatively conditioned normal velocity field. Initially, the vortex tubes near the inlet boundary are primarily in a 2-D form and rapidly become wavy due to the mode resonance of the oblique waves. Then the wavy spanwise vortex filaments either lift up or sweep down, and are stretched into staggered Λ-shaped vortices (marked by black arrows) as they are convected downstream, with a passing spatial period of approximately one wavelength of the most unstable oblique mode from linear stability analysis. The Λ-vortices further deform into hairpin-shaped vortices (labelled by black arrows) and finally break up into smaller-scale structures.

In the region farther away from the inlet, the relative positions of the wave and vortical structures become much clearer, e.g. at the streamwise position $x = 50$ (labelled by a black arrow). The 3-D waves, characterised by the conditioned normal velocity, appear between the two legs of the Λ-vortices. As the structures move downstream, the disturbance wave no longer appears as a 3-D wave bulge but is split into two branches that correspond to the adjacent legs of Λ-vortices (see red arrows in figure 6). However, the wave structures, along with the accompanying vortical structures, persist in their downstream movement.

Depicted in figure 7(a–d) are contours of streamwise vorticity overlaid on velocity vectors (v, w) within the slices at four subsequent streamwise locations, which reveal a possible causal relation between local flow events and vortex evolution. For instance, few vortical motions are observed in figure 7(a) despite the presence of relatively small streamwise vorticity. The slice in figure 7(b) cuts through the first set of Λ-vortices.

https://doi.org/10.1017/jfm.2025.10548 Published online by Cambridge University Press

In this region, the positive normal fluid motion within Λ-vortex 1, and the negative normal motion between Λ-vortex 1 and Λ-vortex 2, sustain the local vortical structures. The connection between the normal fluid events and vortex structures is similar to that in the turbulent bursting of wall-bounded flow, i.e. the 'lift-up' and 'sweep-down' events sustaining the existence of streaks. It should be noted that in turbulent bursting of wall bounded flows, the sweep events happen passively as the lift-up events cause momentum loss near the wall. However, in the mixing layer, the lift-up and sweep-down in either positive or negative normal directions is permitted, as there is no wall restriction in the current configuration (this will be discussed in detail in § 5). In figure 7(*c*), the lift and sweep events, along with vortical motions, are further enhanced. A much stronger nonlinearity effect leads to the breakdown of vortices in figure 7(*d*), which indicates that the flow is gradually evolving into a turbulent state.

In addition to the results presented above, the visualisation of a wave/vortex co-existence state under a different condition is also carried out to explore the effects of random disturbance at the inlet. For clarity, the results and corresponding discussions will be published separately in another paper.

3.2. *Co-evolution of wave and vortex structures*

In this subsection, the spatiotemporal evolutions of both the wave and vortex structures are explored by involving Lagrangian elements driven by the same instantaneous Eulerian fields of Case1. This analysis can help to provide insights into the dynamics of different coherent structures.

Displayed in figure 8 are four sets of timelines (i.e. the 'digital hydrogen bubbles' $\boldsymbol{L}(t)$), which are initially released at different streamwise locations ($x_0 = 50$, 100 and 200) with a constant release time interval. It should be mentioned that the timelines only span a range $z \in [5.0, 30.9]$ in the z-direction to save tracking time.

The first set of timelines is obtained by releasing at $x = 50$, which evolves into a wave-like staggering pattern as shown in figure 8(*a*). The streamwise and spanwise distances between the adjacent 'peaks' or 'valleys' of 3-D waves are approximately 20 and 15, respectively. The amplitudes of the wavy bulges gradually increase in both of the normal directions (see the variation of the colour bars). Furthermore, the timelines in front of the bulge are denser than those in other regions, which results from the deficit of streamwise velocity. In this region, the evolution of material lines is mainly controlled by the tilting mechanism, as illustrated in figure 9(*a*). Depicted in figure 8(*b*) are another set of timelines released at $x = 100$. As staggered wavy bulges start to deform, their amplitudes are further magnified. Figure 8(*c*,*d*) show timelines released much further downstream at $x = 200$, where the material lines appear inclined and twisted, indicating that Λ- or hairpin-shaped vortex patterns become significantly dominant. Figure 8(*d*) presents an upside-down version of the timeline in figure 8(*c*), indicating that hairpin vortices grow on both sides of the mixing centre layer in the normal direction, which differs from boundary layers and will be discussed later.

Particles are not simply oscillating upwards or downwards, but concentrate into inclined ribs through vortex stretching mechanism (as illustrated in figure 9*b*). Due to stronger vortical motions, the particle concentration is observed to be more rapid and compact in figure 8(*c*,*d*) than in figure 8(*b*).

Figure 10 shows evolutions of the material surface $\boldsymbol{M}(t)$ superimposed with the iso-surface of the second invariant of velocity gradient Q at different time t. As illustrated by the Eulerian patterns in § 3.1, we know that the initial shear layer (homogeneous in streamwise and spanwise directions) is susceptible to redistribution and deformation

https://doi.org/10.1017/jfm.2025.10548 Published online by Cambridge University Press

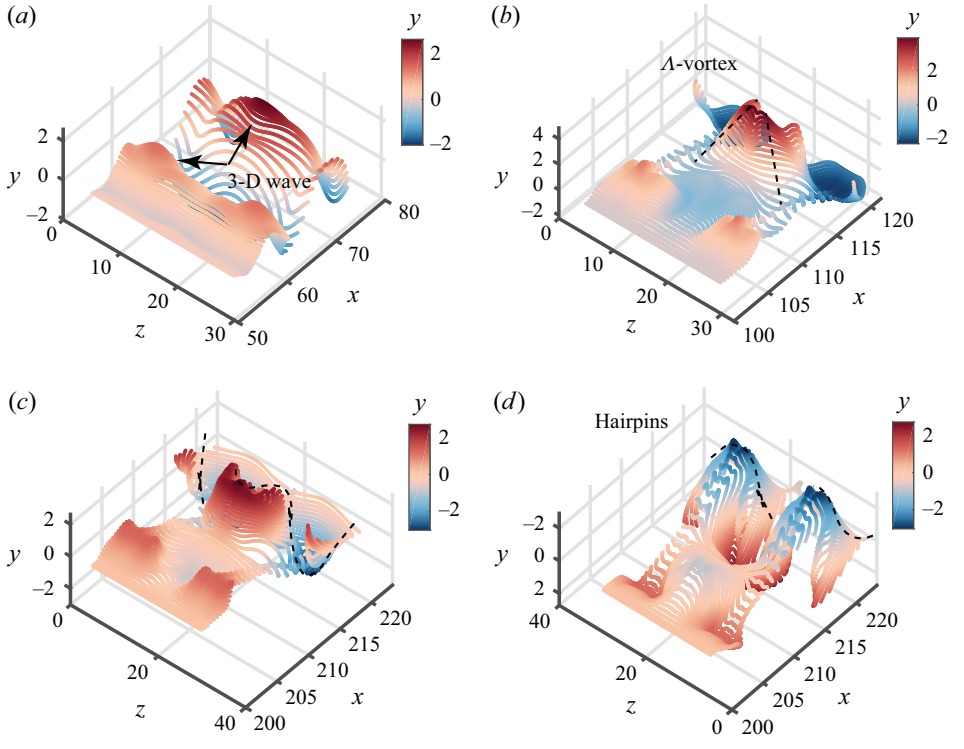


Figure 8. Timelines released simultaneously at the same normal position ($y_0 = 0.18$) but with different streamwise locations: (*a*) $x_0 = 50$, (*b*) $x_0 = 100$, (*c*,*d*) $x_0 = 200$. The timelines are coloured by the local normal position y of particles to visualise the spatial metamorphosis of material lines caused by the local flow structures. Note that (*d*) presents the same timelines as (*c*) but with the y-axis inverted.

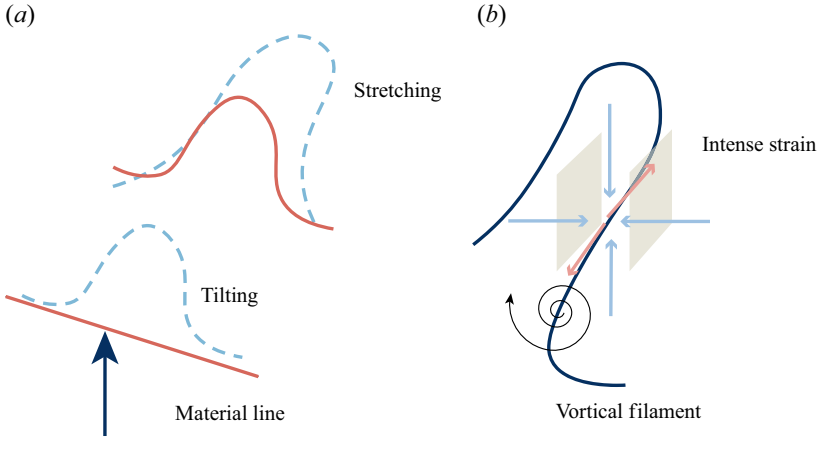


Figure 9. Illustration of (*a*) tilting and stretching of a material line, and (*b*) stretching of a vortical filament.

due to the presence of 3-D disturbance waves and vortical structures, as evidenced by the wrinkling Lagrangian structures. From figure 10(*a–c*), the general process for a 3-D perturbation wave to trigger the development of hairpin vortices can be described as follows.

https://doi.org/10.1017/jfm.2025.10548 Published online by Cambridge University Press

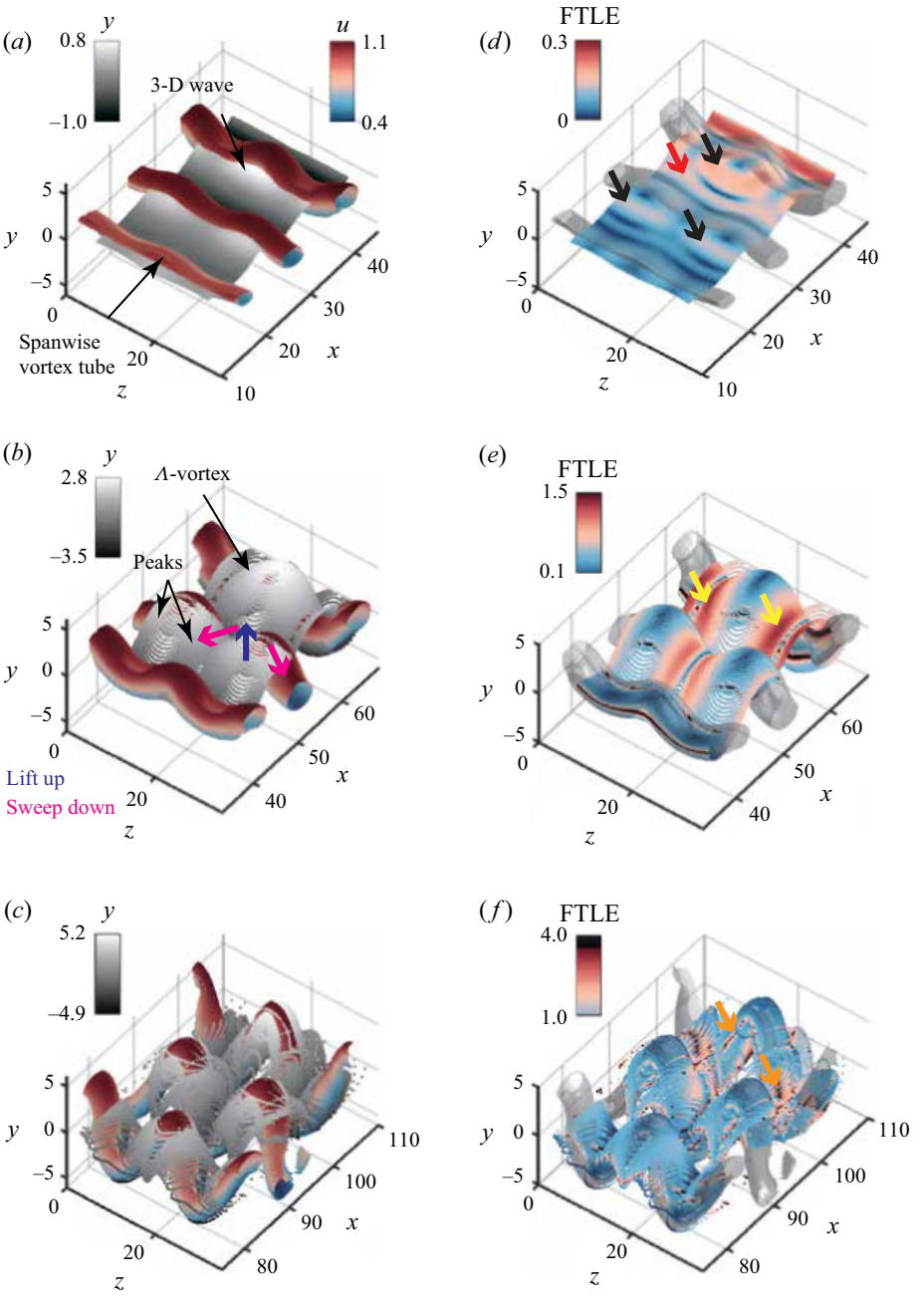


Figure 10. Evolution of a material surface (in black and white) initiated at $y_0 = 0$, $x_0 \in [5, 35]$, $z_0 \in [5, 30]$ for Case1: (*a*,*d*) $t - t_0 = 10.0$, (*b*,*e*) $t - t_0 = 43.5$, and (*c*,*f*) $t - t_0 = 98.0$. (*a*–*c*) The iso-surfaces of $Q = 4 \times 10^{-3}$ are superimposed and coloured by the streamwise velocity u; the colour map at the top-left corner of each panel reflects the values of normal coordinate y. (*d*–*f*) The same Q iso-surfaces are visualised in grey, and the colour map represents the FTLE field Λ_{t-T}^{t} for material surfaces at t with fixed integration time $T = 2$.

https://doi.org/10.1017/jfm.2025.10548 Published online by Cambridge University Press

Shown in figure 10(*a*) is the instantaneous shape of a material surface near the inlet, where the material surface undergoes subtle normal deformation, indicating that the staggered 3-D wave structures are dominant in this region. The wavy vortical structures in the same region are large-scale spanwise vortex tubes, which are the result of motion of 3-D disturbance waves. The amplitude of the 3-D waves increases as the material surface moves downstream (see figure 10*b*). This increase in amplitude is consistent with the fluid lift-up or sweep-down events shown in figure 6. At this stage, Λ-vortices form, with their two legs embracing a single 3-D wave.

With continuous deformation of the material surface, the 3-D bulge no longer maintains its original shape but splits into two 'peaks' in the spanwise direction (see arrows in figure 10*b*). This phenomenon can serve as evidence that the lateral motions from vortical flows are strong enough in this region. As the flow structures continue to develop downstream, the Λ-vortices have gradually evolved into hairpin-shaped structures in this region. It becomes almost impossible to distinguish between the material surface and the Eulerian vortical structures, as nearly all particles engage with neighbouring vortical structures (see figure 10*c*).

3.3. *Wave–vortex interactions*

In § 3.1, it is observed that the transitional section of the mixing layer is dominated by both wave and vortex structures. In § 3.2, it is further explained that the two types of structures evolve with a coupling mechanism. In the early stage of transition, the wave–vortex relation is assumed to be causal rather than merely correlated. In this subsection, evidence will be presented to further demonstrate that the wave and vortex structures interact with each other through local strain rate fields. The target is realised by tracking relevant quantities by interpolating local flow information onto an evolving material surface.

Depicted in figure 10(*d–f*) are evolutions of the FTLE field as introduced in § 2.3, which measures the innate deformation of a material surface. The scalar field is carried by the same material surface $\boldsymbol{M}(t)$ as shown in figure 10(*a–c*) and evaluated in § 3.2. Through the forward integration as introduced in § 2.3, 'repelling' Lagrangian structures are obtained, which are represented by the local maximum magnitude of FTLE fields. The local maximum can be seen as ridges on the material surface and labelled by the coloured arrows in these figures. At the early stage of transition (see figure 10*d*), one local maximum of the FTLE is observed encircling the 'mountainside' of the 3-D wave (labelled by the black arrow), with another local maximum on the ridges connecting neighbouring wave peaks (labelled by the red arrow). Global maxima occur at valleys between wave peaks, indicating that the stretching is most intense in these areas. In figure 10(*e*), part of the local maxima of FTLE migrate to the 'mountain flanks' of the wave peaks (labelled by the yellow arrows). These regions on $\boldsymbol{M}(t)$ are also places where the legs of inclined Λ-vortices penetrate the material surface, implying that the local maxima of the FTLE are indeed projections of the detected 'repelling' Lagrangian structures (Λ-vortices herein). In figure 10(*f*), the maxima of the FTLE appear on boundaries of the vortices (labelled by the orange arrows), which represent vortex stretching on the rotation edges. Additionally, particles distributed within the 'bulge' zones are found much less in this stage because those particles have been causally attracted into vortical structures. It should be noted that the number of particles used for Lagrangian tracking is insufficient. If a sufficiently large number of particles are continuously injected, the 'bulge' region should appear as a continuous surface.

The above analysis unveils the kinematic stretching and deformation of Lagrangian structures. However, it is also appealing to consider what happens in the neighbourhood

https://doi.org/10.1017/jfm.2025.10548 Published online by Cambridge University Press

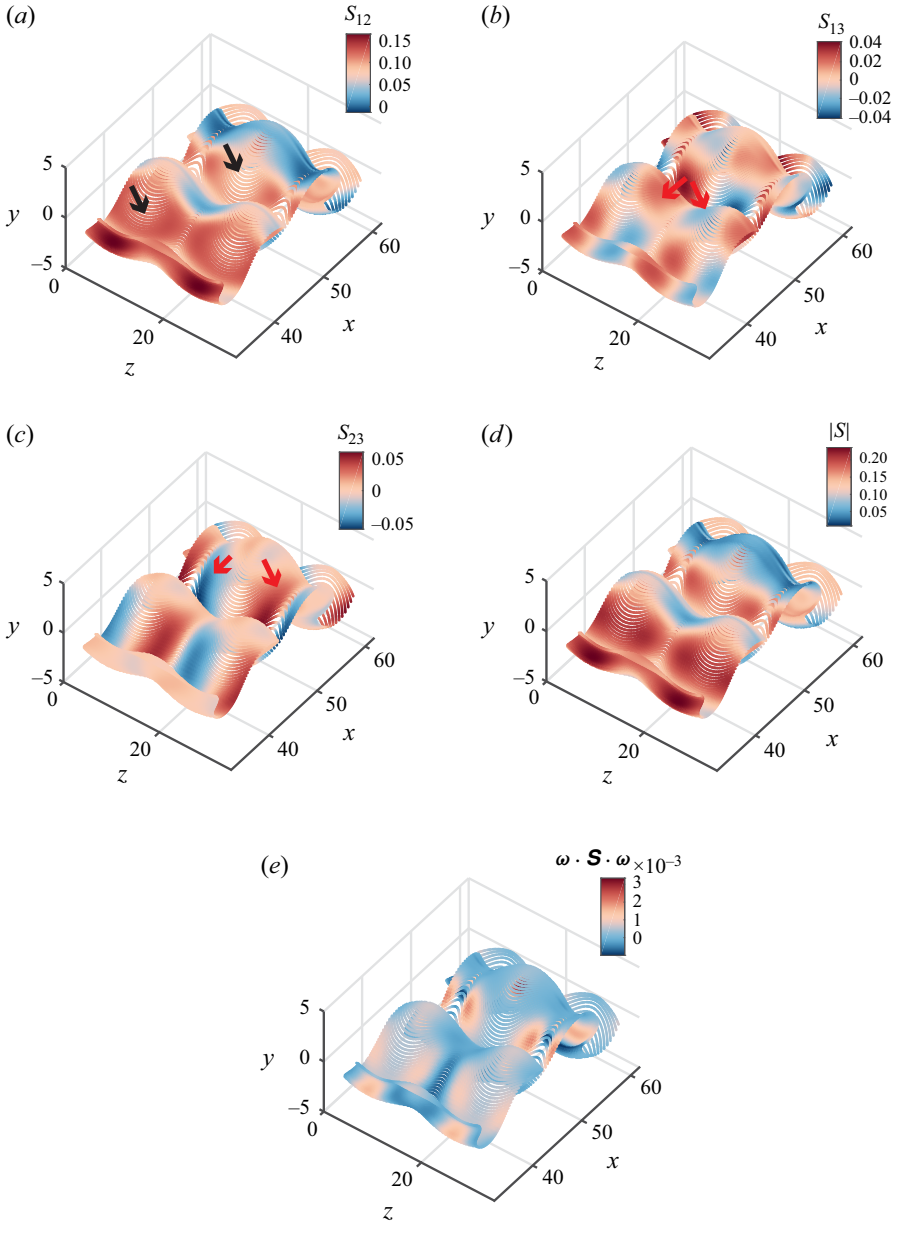


Figure 11. The material surface at $t - t_0 = 35$, which is initiated at $y_0 = 0$, $x_0 \in [5, 35]$, $z_0 \in [5, 30]$ for Case1 (same as in figure 10), and coloured by different components of the strain rate tensor: (*a*) S_{12}, (*b*) S_{13}, (*c*) S_{23}, (*d*) $|\boldsymbol{S}|$, the norm of the strain rate tensor, and (*e*) $\boldsymbol{\omega}\cdot\boldsymbol{S}\cdot\boldsymbol{\omega}$, the stretching term of enstrophy.

of the 2-D surface in 3-D space, where high strain rate layers may function as a 'catalyst' by dynamically interacting with both the waves and vortices. Displayed in figure 11(*a–d*) are distributions of the strain rate related quantities on the material surface. It is found that higher $S_{12} = 1/2(\partial u/\partial y + \partial v/\partial x)$ appears on the 'hillsides' of wave packets, especially on the wave-front regions (labelled by black arrows). Both $S_{13} = 1/2(\partial u/\partial z + \partial w/\partial x)$ and $S_{23} = 1/2(\partial v/\partial z + \partial w/\partial y)$ are observed to be concentrated in the wave-flank zones (labelled by red arrows) but in opposite strain directions. In addition, it turns out that

https://doi.org/10.1017/jfm.2025.10548 Published online by Cambridge University Press

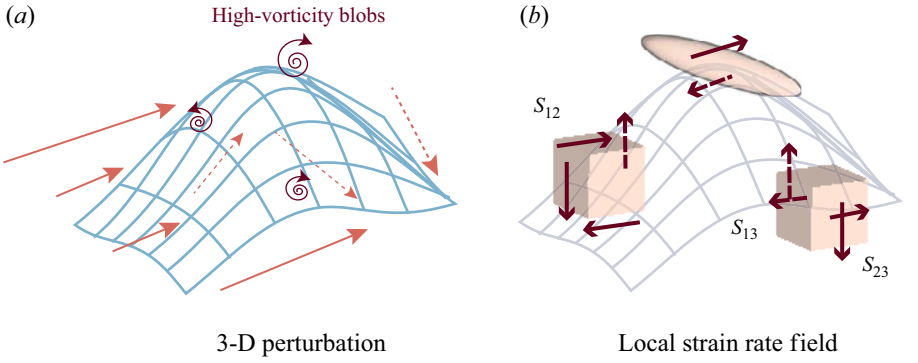


Figure 12. Illustration of (*a*) local motion of fluids around a 3-D wave, and (*b*) strain rate state around a 3-D wave.

the distribution of S_{12} is most similar to that of the magnitude $|\boldsymbol{S}|$ by comparing different components of the strain rate tensor (S_{12}, S_{12} and S_{23}) with $|\boldsymbol{S}|$. The large magnitude of the strain rate also indicates a high dissipation rate in such regions. Figure 11(*e*) displays the flux contribution by stretching to the change of enstrophy. The distribution of $\boldsymbol{\omega}\cdot\boldsymbol{S}\cdot\boldsymbol{\omega}$ is quite similar to that of S_{13} or S_{23}, indicating that the local strain rate field, induced by wave motions rather than vorticity self-induction, is an effective contributor to the formation of vortical structures in the early stage of transition.

It should be remarked that the geometric form of the material surface at this moment comes from the integrated effect of local strain and vorticity from the moment when the material surface is initially released. The dynamical process can be interpreted by the relation between Lagrangian and Eulerian stretching, which formulates as the evolution of the deformation gradient tensor $F_{ij}(t) = \nabla F^{t}_{t_0} = \partial X_i(t, \boldsymbol{X}_0)/\partial X_{0j}$:

$$\frac{\mathrm{d}F_{ij}(t)}{\mathrm{d}t} = G_{ik}(t)\, F_{kj}(t) = (S_{ik} + A_{ik})\, F_{kj}(t), \tag{3.3}$$

in which G_{ik} is the velocity gradient tensor, which can be decomposed into a symmetric part (i.e. the strain rate tensor S_{ij}) and an antisymmetric part (i.e. the rotation tensor A_{ij}). Equation (3.3) suggests that the deformation of the material surface is controlled by both strain and rotation parts of the velocity gradient, even though in the early stages of the evolution (see figure 10*a*,*b*), it undergoes more metamorphosis due to the straining effect, while the rotation becomes stronger and causes a single wave peak to break into two parts at later stages (see figure 10*c*,*d*), as will be discussed later.

Based on the above results, the process where a 3-D wave interacts dynamically with adjacent Λ-vortices (see figure 12*a*) through immediate high shear (strain rate) structures (figure 12*b*) can be interpreted as follows. Ejection of fluids (termed as a 3-D perturbation wave in figure 12*a*,*b*) alters the motion of local fluids, which should be substantially convected downstream. Surrounding the 3-D wave 'mountain' (represented by the meshed surface in the illustration), the fluids originating from upstream (straight solid arrows) are obstructed on the 'windward' side, and experience a decrease in streamwise velocity. The decelerated fluids either participate in the ejection process or circumvent the wave (straight dashed arrows). Furthermore, mass conservation requires that the position vacated by the injected fluids must be filled by fluids from the ejection terminus. These reverse motions lead to the formation of a high-shear layer with enhanced vorticity concentration. As illustrated in figure 12(*b*), the sketched local strain rate field on

https://doi.org/10.1017/jfm.2025.10548 Published online by Cambridge University Press

the 'windward' side is dominated by the high-shear components $\partial v/\partial x$ and $\partial u/\partial y$, which correspond to high magnitude of S_{12} in this region. Similarly, at the peak of the 3-D wave where $\partial v/\partial x$ becomes weak, the shear component $\partial u/\partial y$ along with lateral stretching makes spanwise vorticity concentrated in this region, which explains the formation of a Λ-vortex head. At flanks of the 3-D wave, an ejecting/sweeping event causes high shear $\partial v/\partial z$, while the spanwise gradient of u causes high shear $\partial u/\partial z$, which gives rise to the large magnitudes of S_{23} and S_{13}, respectively. It is worth noting that the initial high-vorticity blobs (sketched by swirling arrows) are born in the 3-D wave flanks especially due to the local shear $\partial v/\partial z$ (the main contribution to streamwise vorticity concentration). The blobs are further stretched by the global mean shear, which will be explained in § 4.2.

4. Statistical studies

4.1. *Energy evolution*

The streamwise evolutions of kinetic energy in Fourier modes of Case1 are calculated to statistically investigate the dynamic growth of disturbance waves, which have been visualised by material surfaces in § 3.2. The temporal–spatial kinetic energy spectrum can be defined in the form

$$E(\omega, \beta) = \int_{-L_y/2}^{L_y/2} \tilde{u}(\omega, \beta)\, \tilde{u}^c(\omega, \beta)\, \mathrm{d}y, \tag{4.1}$$

where the superscript 'c' denotes the complex conjugate. The streamwise evolutions of the frequency spectrum and wavenumber spectra are shown in figures 13(a) and 13(b), respectively. As is seen in figure 13(a), the kinetic energy is concentrated and distributed near the fundamental frequency $\omega_0 = 0.41$ of disturbance waves. High-order harmonic frequencies $3/2\omega_0$ and $5/2\omega_0$ gradually come into being due to wave resonance during the very early stage of transition ($x < 50$). It can also be observed that the kinetic energy is mainly concentrated at the wavenumber $\beta_0 = 0.36$ of oblique disturbance. Harmonic wavenumbers such as $2\beta_0$ and $3\beta_0$ become important where $x > 100$, as shown in figure 13(b). For those high-order harmonic spanwise structures, the third harmonic wave increases most rapidly, and becomes secondary to the fundamental wavenumber within the region $100 < x < 400$. Much farther downstream, the spectral energy gradually spreads into a wider wavenumber range, although the mode with the fundamental frequency and wavenumber still dominates.

To investigate the mode–mode energy competition, the evolutions of spectral kinetic energy for several selected Fourier modes from figures 13(a) and 13(b) are shown in figure 13(c). It is suggested that the growth of energy in these selected modes could be generally divided into three stages. In the first stage ($0 < x < 50$), i.e. the region very close to the inlet, energy of all modes experiences a transient increase, except that of the 2-D disturbance mode (1, 0), which undergoes a rapid increase first and then decreases. In the following stage ($50 < x < 150$), the energy of the 3-D oblique mode (1, 1) and 2-D disturbance mode (1, 0) both grow slowly. The energy of the mode with frequence (3/2, 1) increases in a similar way to the (1, 1) mode. Other high-order harmonic modes such as (1, 2) and (1, 3) also experience growths in the second stage, which are much more rapid than the fundamental modes.

The energy evolutions examined above indicate that the excitation of 3-D disturbances with the 2-D field would eventually establish a positive feedback loop and lead to the self-sustained simultaneous growth of 2-D and 3-D waves. The final stage of energy

https://doi.org/10.1017/jfm.2025.10548 Published online by Cambridge University Press

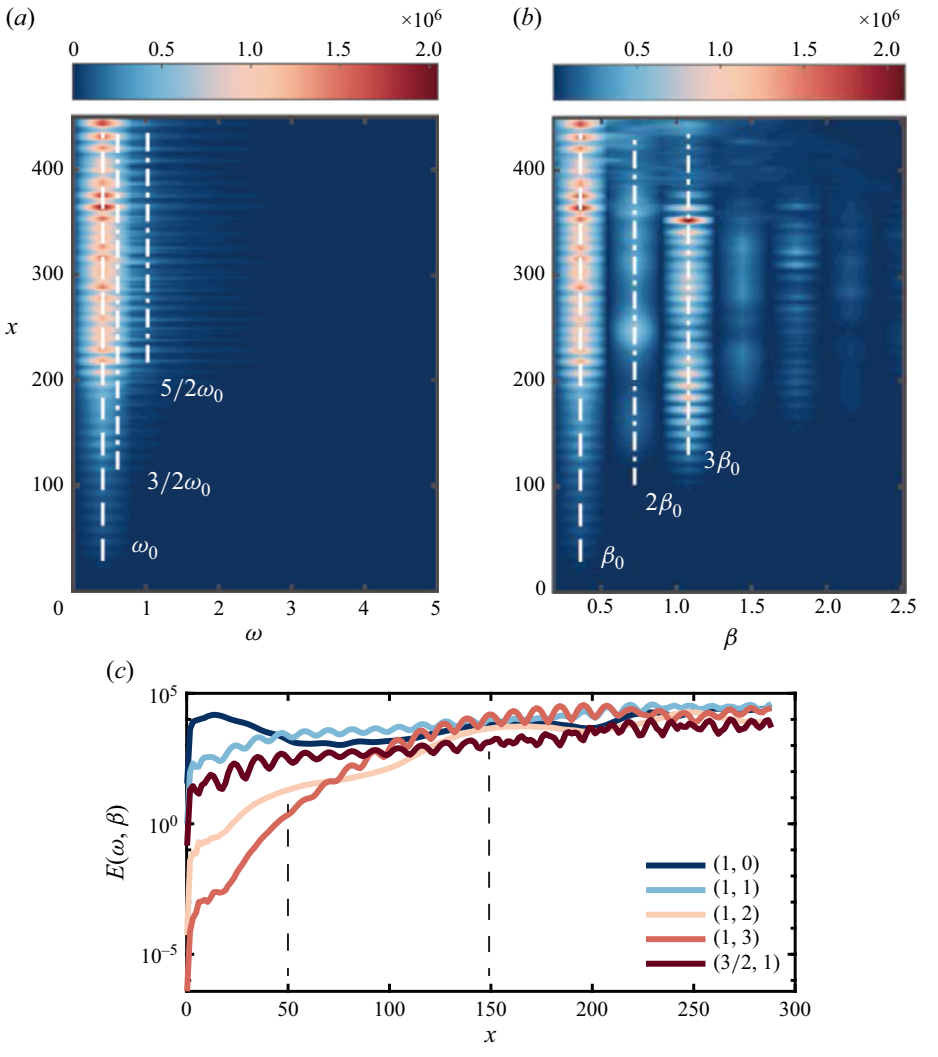


Figure 13. Streamwise evolutions of spectral kinetic energy $E(\omega, \beta)$: (*a*) frequency spectrum at $\beta = \beta_0$, (*b*) spanwise wavenumber spectrum at $\omega = \omega_0$, and (*c*) spectral energy of selected modes. Here, the frequency and spanwise wavenumber spectra are rescaled by those of the fundamental mode $E(\omega_0, \beta_0)$ at the inlet.

development ($x > 150$), shown in figure 13(*c*), is characterised by much more moderate growth, and the energy contained in each mode tends to be the same order of magnitude. Meanwhile, the wave–vortex interaction begins at approximately $x = 150$ due to the appearance of a Λ-vortex (accompanied by surges of high-order harmonic modes of (1, 2) or (1, 3)). This is consistent with the visualisation in figure 6 or figure 10, indicating that nonlinear effects become dominant in this region.

From the perspective of energy feedback, the 3-D wave mode (1, 1) takes the lead in energy growth within the range $50 < x < 150$, during which localised high shear emerges due to the amplification of 3-D waves. The 2-D wave mode (1, 0) excites strong energy transfer from the mean flow into the 3-D wave since its amplitude is sufficiently large initially (see e.g. Croswell 1985; Herbert 1988). While some portions of this excited energy increase the amplitude of mode (1, 1), other parts are dissipated during the evolution. Once

https://doi.org/10.1017/jfm.2025.10548 Published online by Cambridge University Press

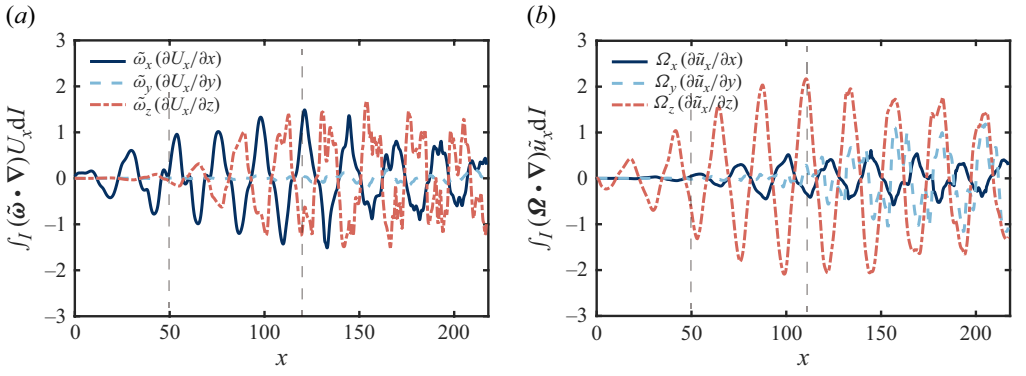


Figure 14. Streamwise evolution of the right-hand-side contributions of the governing equation for fluctuating vorticity: (*a*) stretching and twisting of the fluctuating vortex by the mean flow field, and (*b*) stretching and twisting of the mean vortex by the fluctuating velocity field. Here, I denotes the region of the streamwise flux integral.

the energy of mode (1, 1) attains a sufficiently large value ($x > 50$), the energy of mode (1, 0) shows a tendency for slow increase again.

It needs to be pointed out that the evolutions of energy spectra in figure 13 are indeed a time-averaged result. The streamwise wavy phenomenon of these single-mode energy spectra comes from periodic structures in that dimension. The averaging operation remarkably reduces streamwise oscillation of the energy spectra for modes (1, 0) and (1, 2), while inconspicuously flattening other modes because these modes are travelling with different phase velocities.

4.2. *Formation of streamwise vorticity*

In addition to the growth of wave energy, it is also necessary to analyse the dynamical process through which the oblique waves trigger the formation of Λ-vortices as visualised in § 3.3. To achieve this, the flow field is decomposed into a mean component and a fluctuating component to distinguish the wave part from other aspects of flow, i.e.

$$\begin{aligned} \boldsymbol{u}(\boldsymbol{x}, t) &= \boldsymbol{U}(\boldsymbol{x}, t) + \tilde{\boldsymbol{u}}(\boldsymbol{x}, t), \\ \boldsymbol{\omega}(\boldsymbol{x}, t) &= \boldsymbol{\Omega}(\boldsymbol{x}, t) + \tilde{\boldsymbol{\omega}}(\boldsymbol{x}, t). \end{aligned} \tag{4.2}$$

By substituting the above decomposition into the dynamic equation of vorticity (2.12), one can obtain the governing equations of both mean vorticity and fluctuating vorticity. Detailed derivations for these equations are given in Appendix B. The interaction between disturbance and vorticity can be represented by terms in right-hand side of the disturbance vorticity equation (B2). Here, the focus is placed on contributions to the change in streamwise vorticity from fluctuating vortex stretching by the mean strain rate $(\tilde{\boldsymbol{\omega}}\cdot\nabla)\boldsymbol{U}$, and mean vortex stretching by fluctuating strain rate $(\boldsymbol{\Omega}\cdot\nabla)\tilde{\boldsymbol{u}}$:

$$\begin{aligned} \frac{\partial \tilde{\omega}_x}{\partial t} \sim{}& \tilde{\omega}_x \frac{\partial U_x}{\partial x} + \tilde{\omega}_y \frac{\partial U_x}{\partial y} + \tilde{\omega}_z \frac{\partial U_x}{\partial z} \\ &+ \Omega_x \frac{\partial \tilde{u}_x}{\partial x} + \Omega_y \frac{\partial \tilde{u}_x}{\partial y} + \Omega_z \frac{\partial \tilde{u}_x}{\partial z}. \end{aligned} \tag{4.3}$$

The right-hand side of (4.3) can be divided into two parts, i.e. stretching/bending of the fluctuating vorticity by the mean velocity field, and stretching/bending of the mean vorticity by the fluctuating velocity field. Shown in figure 14 are streamwise fluxes of the

https://doi.org/10.1017/jfm.2025.10548 Published online by Cambridge University Press

six terms in (4.3), which are calculated by a surface integral over y–z slices at each x position. Note that these terms are integrated within a region (denoted by I) that covers one leg of the streamwise vortex pair.

As discussed previously, 3-D waves are introduced as inflow disturbance, and their growth is correlated with mode interactions. Now we further demonstrate the direct consequence of disturbance wave amplification in figure 14, i.e. the creation of Λ-vortices in locally disturbed strain rate fields. It is also demonstrated that the high-shear layers with enhanced vorticity are generated by interaction of waves with the mean flow. Figure 14 shows that the primary contribution to the generation of streamwise vorticity in the region $x < 50$ comes from $\tilde{\omega}_x(\partial U_x/\partial x)$ (solid line in figure 14*a*) and $\Omega_z(\partial \tilde{u}_x/\partial z)$ (dot-dashed line in figure 14*b*). The former represents the stretching of streamwise fluctuating vorticity by mean streamwise velocity gradient; this is the consequence of decrease in streamwise velocity caused by 3-D wave perturbation, as illustrated in figure 9(*a*). The latter comes from the tilting of mean spanwise vorticity Ω_z by spanwise fluctuating shear $\partial \tilde{u}_x/\partial z$, which is also the effect of the 3-D wave motion. Therefore, it is the wave property of $\tilde{u}_x$ with strong oscillations that results in the streamwise amplification of vorticity flux.

In the region $50 < x < 120$, contributions from other terms gradually increase, corresponding to the second stage of mode growth in figure 13. For example, as shown in figure 14(*a*), the tilting of spanwise vorticity fluctuation $\tilde{\omega}_z$ by mean shear $\partial U_x/\partial z$ (dot-dashed line) starts to be intensified. Meanwhile, the stretching of mean streamwise vorticity Ω_x by fluctuating normal strain rate $\partial \tilde{u}_x/\partial x$ (solid line in figure 14*b*) and the tilting of normal mean vorticity Ω_y by fluctuating shear $\partial \tilde{u}_x/\partial y$ (dashed line in figure 14*b*) are also enhanced. This indicates that the growth of perturbation waves leads to local redistribution of the strain rate field, and the shear parts of strain rate field give rise to quasi-streamwise vortex structures. In the region $x > 120$, the evolution enters the nonlinear development stage and tends to saturate downstream. This saturation can also be observed in the same region of figure 13, where different modes become equally competitive, and the turbulent motion is sustained by energy exchanges among these modes (Li *et al.* 2021).

4.3. *Role of high strain rate*

Based on the analysis of wave–vortex interaction in § 3.3, it is found that fluid layers of high strain rate (S_{12}, S_{13}, S_{23} or $|\boldsymbol{S}|$) are typically preserved surrounding the wave structure, which are the regions where vortex structures are nurtured (as illustrated in figure 12(*c*,*d*) and depicted in figure 11). According to (2.14), the production of enstrophy from vortex stretching/tilting is governed by the alignment between the vorticity vector and eigenvectors of the strain rate tensor $\beta_i \cos^2\langle \boldsymbol{\omega}, \boldsymbol{\Lambda}_i \rangle$. Since the dynamics of $\boldsymbol{S}$ and $\boldsymbol{\omega}$ are coupled with each other, the conditional statistics of the preferential alignment upon the magnitude of strain rate tensor $|\boldsymbol{S}|$ are carried out as a validation test.

As displayed in figure 15, the probability density function (p.d.f.) of the cosine of the angle between the vorticity vector and intermediate eigenvector ($\cos\langle \boldsymbol{\omega}, \boldsymbol{\Lambda}_2 \rangle$) shows strong peaks at 1 and -1, indicating that the most likely behaviour involves considerable alignment with $\langle \boldsymbol{\omega}, \boldsymbol{\Lambda}_2 \rangle = 0°$ and 180°. This observation is consistent with the findings in homogeneous shear turbulence (Ashurst *et al.* 1987) and stratified shear turbulence (Jiang *et al.* 2023). Meanwhile, the corresponding p.d.f.s of $\cos\langle \boldsymbol{\omega}, \boldsymbol{\Lambda}_i \rangle$ conditioned on $|\boldsymbol{S}|^2 > \langle |\boldsymbol{S}|^2 \rangle$ are calculated to highlight the effect of high strain rate, where $\langle |\boldsymbol{S}|^2 \rangle$ is the averaged stain rate value over the entire domain for statistical analysis. It turns out that the preferential alignments increase with the strength of strain rate in both selected regions (figure 15*a*,*b*), suggesting that turbulence is more easily generated in high strain

https://doi.org/10.1017/jfm.2025.10548 Published online by Cambridge University Press

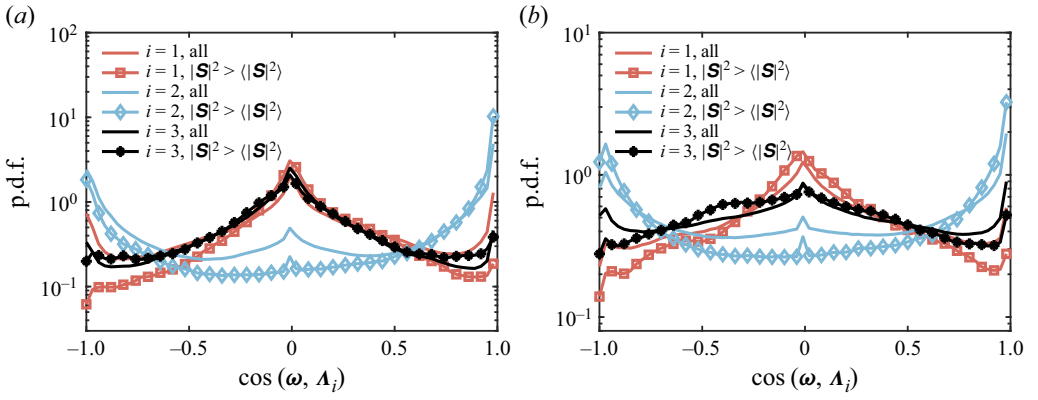


Figure 15. The p.d.f.s of the cosine of the angle between the vorticity vector ω and eigenvectors Λ_i of the strain rate tensor within two selected regions: (*a*) $50 < x < 120$ and (*b*) $150 < x < 220$. Lines with symbols represent the p.d.f.s conditioned on the strength of strain rate $|\boldsymbol{S}|^2 > \langle|\boldsymbol{S}|^2\rangle$.

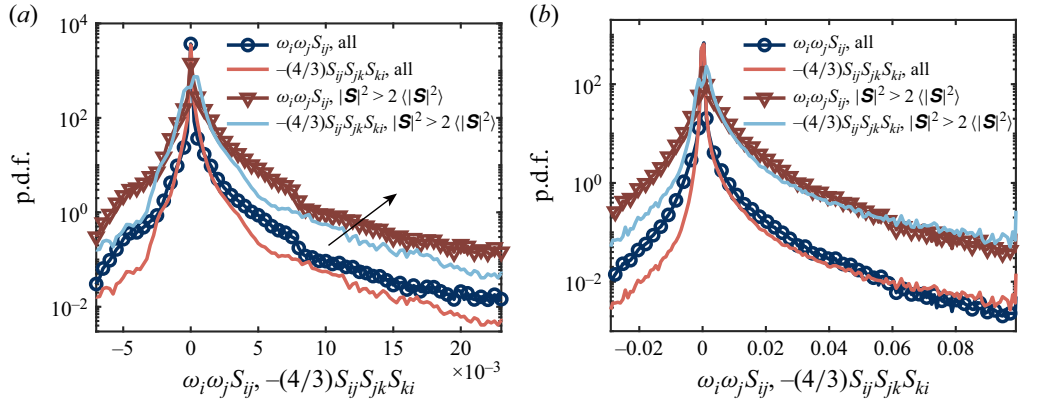


Figure 16. The p.d.f.s of $\omega_i\omega_j S_{ij}$ and $-(4/3)S_{ij}S_{jk}S_{ki}$ within two selected regions: (*a*) $50 < x < 120$ and (*b*) $150 < x < 220$. The p.d.f.s conditioned on high strain rate are also plotted for comparison.

rate regions. By comparing figures 15(*a*) and 15(*b*), it is found that the margin p.d.f. of $\cos\langle\boldsymbol{\omega}, \boldsymbol{\Lambda}_2\rangle$ (within either [0.9, 1.0] or [−1.0, −0.9]) is steeper in figure 15(*a*) than in figure 15(*b*), indicating that the preferential alignment of Λ_2 in the wave–vortex interaction stage ($150 < x < 220$) is weaker than that in the wave growth stage ($50 < x < 120$). It is also observed that the effect of high strain rate, which leads to more preferential alignment between the intermediate eigenvector and the vorticity vector, is more pronounced in the region $50 < x < 120$.

It is also appealing to consider the effect of high strain rate on the production of enstrophy $\boldsymbol{\omega}^{\mathrm{T}}\boldsymbol{S}\boldsymbol{\omega}$ (or $\omega_i\omega_j S_{ij}$) and production of strain rate $S_{ij}S_{jk}S_{ki}$ within the two selected regions. Depicted in figure 16(*a*,*b*) are p.d.f.s and conditional p.d.f.s (upon the strain rate) of the two terms. These distributions are all positively skewed, indicating a net production of both enstrophy and strain rate from the early stage of transition to the late stage of flow development. Conditional samplings of $\omega_i\omega_j S_{ij}$ and $-(4/3)S_{ij}S_{jk}S_{ki}$ on high strain rate ($|\boldsymbol{S}|^2 > 2\langle|\boldsymbol{S}|^2\rangle$) reveal that both quantities become more intermittent and more positively skewed (the variations are marked by a black arrow). It is further

https://doi.org/10.1017/jfm.2025.10548 Published online by Cambridge University Press

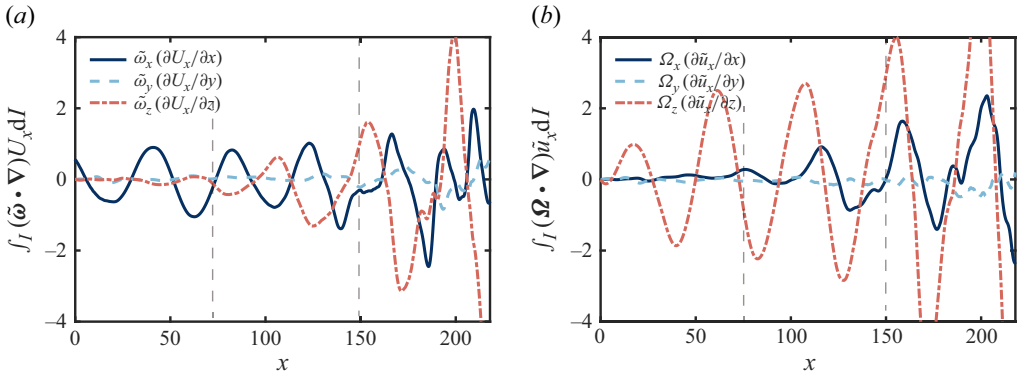


Figure 17. Streamwise evolution of the right-hand-side contributions of the governing equation for fluctuating vorticity at the convective Mach number $Mc = 1.4$: (*a*) stretching and twisting of the fluctuating vortex by the mean flow field, and (*b*) stretching and twisting of the mean vortex by the fluctuating velocity field. Here, I denotes the region of the streamwise flux integral.

identified that the ratio of $\omega_i\omega_j S_{ij}$ to $-S_{ij}S_{jk}S_{ki}$ is consistent with the reported value 4/3 for homogeneous isotropic turbulence (Lawson & Dawson 2015).

By comparing figures 16(*a*) and 16(*b*), it is found that the generations of enstrophy and strain rate are relatively weak during the early transition phase ($50 < x < 120$), but increase approximately by four times in the late transition stage ($150 < x < 220$). The reason for this phenomenon lies in the enhancement of the stretching term as highlighted in figure 10(*d–f*). Furthermore, it is observed that the p.d.f.s become a little more 'symmetric' downstream, which could be the consequence of nonlinearity. These conditional results underscore that enstrophy tends to be generated in regions of intense strain rate, even though the localised enhancement in strain originates from the motion of 3-D waves.

4.4. *Effect of convective Mach number*

To shed light on the effect of compressibility upon the spatial development of a transitional mixing layer, statistical studies are conducted for the test case with convective Mach number $Mc = 1.4$. Shown in figures 17(*a*) and 17(*b*) are the streamwise variations of stretching and twisting of the fluctuating vortex by the mean flow field, and stretching and twisting of the mean vortex by the fluctuating velocity, respectively. It turns out that the mixing layer grows at a lower frequency (i.e. the quasi-periodic structures have larger wavelength) in comparison with the case $Mc = 0.7$. Analogous to the situation at $Mc = 0.7$, the primary contribution to the generation of streamwise vorticity in the early transition region ($x < 75$) still comes from $\tilde{\omega}_x(\partial U_x/\partial x)$ (solid line in figure 17*a*) and $\Omega_z(\partial \tilde{u}_x/\partial z)$ (dot-dashed line in figure 17*b*). Besides, contributions from other terms gradually increase in the region $75 < x < 150$, and the evolution enters the nonlinear development stage after $x > 150$, similar to the case $Mc = 0.7$. The main difference lies in the tilting of the mean spanwise vorticity by spanwise fluctuating shear $\Omega_z(\partial \tilde{u}_x/\partial z)$, which is even stronger than that in the low convective Mach number case. This phenomenon actually confirms the dominant role of oblique instability in the high convective Mach number regime (Sandham & Reynolds 1991).

Depicted in figures 18(*a*) and 18(*b*) are p.d.f.s of the alignment between vorticity vector $\boldsymbol{\omega}$ and eigenvectors $\boldsymbol{\Lambda}_i$ of the strain rate tensor within two selected regions for the case $Mc = 1.4$. As can be seen, the p.d.f.s of the cosine of the angle between the vorticity

https://doi.org/10.1017/jfm.2025.10548 Published online by Cambridge University Press

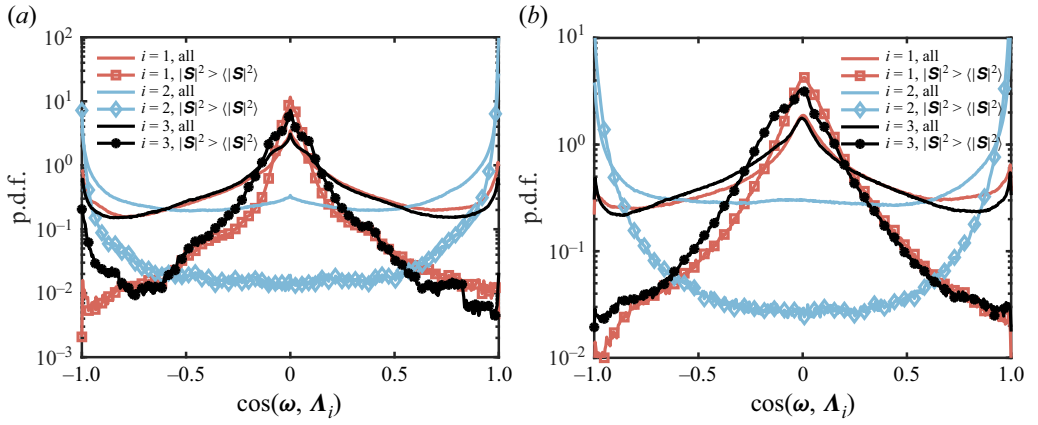


Figure 18. The p.d.f.s of cosine of the angle between vorticity vector $\boldsymbol{\omega}$ and eigenvectors $\boldsymbol{\Lambda}_i$ of the strain rate tensor within two selected regions at the convective Mach number $Mc = 1.4$: (*a*) $50 < x < 150$ and (*b*) $200 < x < 300$. Lines with symbols represent the conditional p.d.f.s based on the strength of strain rate $|\boldsymbol{S}|^2 > \langle|\boldsymbol{S}|^2\rangle$.

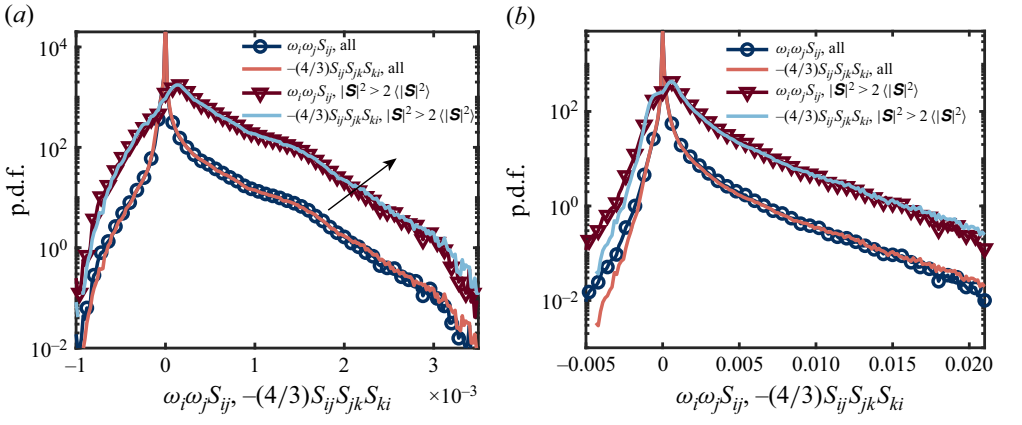


Figure 19. The p.d.f.s of enstrophy production $\omega_i\omega_j S_{ij}$ and strain rate production $-(4/3)S_{ij}S_{jk}S_{ki}$ within two selected regions at the convective Mach number $Mc = 1.4$: (*a*) $50 < x < 150$ and (*b*) $200 < x < 300$. The p.d.f.s conditioned on high strain rate are also plotted for comparison.

vector and intermediate eigenvector ($\cos\langle\boldsymbol{\omega}, \boldsymbol{\Lambda}_2\rangle$) display an increased concentration near 1 and -1 in both selected regions. The increasing trend is even more pronounced in the downstream region, i.e. figure 18(*b*). It is also found that the effect of high strain rate on the preferential alignment is enhanced in the high Mach number case compared to the low Mach number case.

Figures 19(*a*) and 19(*b*) present the p.d.f.s of enstrophy production $\omega_i\omega_j S_{ij}$ and strain rate production $-(4/3)S_{ij}S_{jk}S_{ki}$ within two selected regions for the case $Mc = 1.4$. Basically, the production in both regions decreases by 2/3 compared with that in the case $Mc = 0.7$. Comparisons of conditioned samplings show that the influence of Mach number on the strain rate contribution is limited.

5. Summary and discussions

Based on the results presented in previous sections, it can be inferred that the inhomogeneous strain rate field within the mixing layer primarily arises from the

https://doi.org/10.1017/jfm.2025.10548 Published online by Cambridge University Press

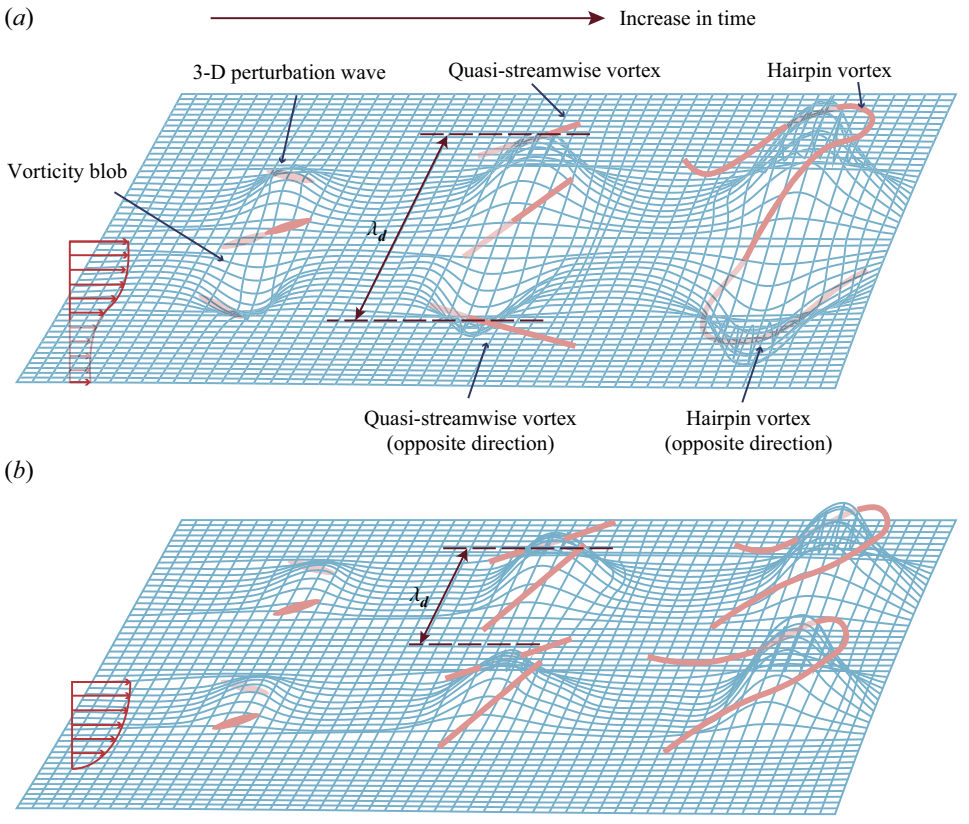


Figure 20. Conceptual models of the early-stage transition based on 3-D waves: (*a*) mixing layer flow with wave and vortex structures depicted within one wavelength in the spanwise direction; (*b*) boundary layer flow with wave and vortex structures displayed within two wavelenghths in the spanwise direction.

interaction of 3-D perturbation waves with the background shear. This interaction results in the formation and concentration of streamwise vorticity. These quasi-streamwise vortex filaments undergo further stretching and twisting, ultimately breaking down into much smaller turbulent structures. Based on these findings, a schematic model is proposed for the evolution of a 3-D wave and its subsequent development into a Λ/hairpin vortex, as illustrated in figure 20(*a*).

5.1. *A comparison with the scenario in boundary layer flow*

Inspired by the hypothesis on the role played by 3-D waves in boundary layer transition (Lee & Wu 2008; Jiang *et al.* 2020*a*), it is suggested that these wave structures serve as pivotal building blocks in laminar–turbulent transition of a compressible mixing layer flow. Jiang *et al.* (2022) also highlighted that the amplification of a 3-D wave as a key initiator of a vortex may be a universal feature of shear-driven turbulence, occurring in both wall-bounded and wall-free configurations.

Although the present study demonstrates a similar role of a 3-D wave in the transition of a mixing layer, it should be noted that the dynamic process for a mixing layer can differ from that for a boundary layer. This discrepancy arises because 3-D waves are allowed to move freely in both vertical directions in the mixing layer, as opposed to being constrained to an impermeable wall. Given a disturbance with the spanwise wavelength λ_d, both the wave and hairpin vortex structures are antisymmetric in the z-direction between

https://doi.org/10.1017/jfm.2025.10548 Published online by Cambridge University Press

the upper and lower parts of the mixing layer (see figure 20*a*). There are two heads (one is on the high-speed side, and the other is on the low-speed side) and four legs (two of them on the high-speed side, and the other two on the low-speed side) within one period of the disturbances. However, given a disturbance with the same spanwise wavelength λ_d, the wave and hairpin vortex structures are symmetric in the flat plate boundary layer. There are one head and two legs within one period of the disturbances (see figure 20*b*).

As a consequence of interaction with the mean shear, disturbances provide aid in triggering the generation of quasi-streamwise vortices and hairpin vortices in the high- and low-speed fluid layers, respectively. Vortices adjacent to each other at different layers, with their heads oreiented in opposite spanwise directions, can be connected by their legs. However, hairpin vortices with a consistent orientation predominate in boundary layer flows. Furthermore, the presence of walls in the boundary layer results in the isolation of quasi-streamwise vortices, with the potential for their legs to interact with each other (e.g. reconnection), while the lifting phenomenon primarily occurs above the hairpin neck (see Zhou *et al.* 1999). It should also be mentioned that the vertical lifting of vortices within the mixing layer may experience suppression to some extent due to the presence of stratification. For example, Jiang *et al.* (2022) demonstrated that the vertical inclination angle for a hairpin vortex in stratified mixing layers is approximately 10°, which is approximately half of what is observed in the present study.

5.2. *The 3-D wave and ejection/sweep of fluids*

In § 3.2, visualisation of typical material surfaces exhibits a continuous metamorphosis from the initially 2-D vortex tubes near the inlet to downstream wavy structures and the consequent staggered Λ-shaped vortices. This reveals a causal relationship between local flow events, characterised by positive and negative vertical fluid motions, and the persistence of vortical structures. In figures 6, 10 and 11, one can clearly observe the localised normal fluid movements, which stem from perturbation 'seeds' introduced at the inlet, and germinate within the background shear.

The $Q2$ ($u' < 0$, $v' > 0$) and $Q4$ ($u' > 0$, $v' < 0$) motions, which are associated with the ejection and sweep events in wall-bounded flow, can similarly serve as a classification of gradient-type motions in the mixing layer. This enables the identification on contributions of the ejection and sweep events to vortex formation and turbulence production. By examining small flow structure units, which encompass individual wave/vortex structure and neighbouring flows, a quadrant analysis is conducted for velocity fluctuations u' and v' across different streamwise regions (see figure 21). To facilitate the differentiation of events occurring at different heights within the mixing layer, the scatter plots in figure 21 are colour-coded to represent deviations of the normal position from the mean position in corresponding regions.

As shown in figure 21(*a*), the circular band of scatter points corresponds to the dominant motion of organised 3-D waves in early transition stage. As Δy increases (from blue to red), the contribution to turbulence production shifts from $Q1$ and $Q3$ events to $Q2$ and $Q4$ events, manifesting that ejection–sweep events happen on both sides of the centreline of the mixing layer. Additionally, the contribution of sweep events decreases away from the mixing centre, with ejection becoming predominant at the upper edge of the mixing region.

As one can see in figure 21(*b*), the quadrant distribution is similar to that in figure 21(*a*), but with more $Q1$ events in the low-speed layer (blue) and more $Q2-Q4$ events in the

https://doi.org/10.1017/jfm.2025.10548 Published online by Cambridge University Press

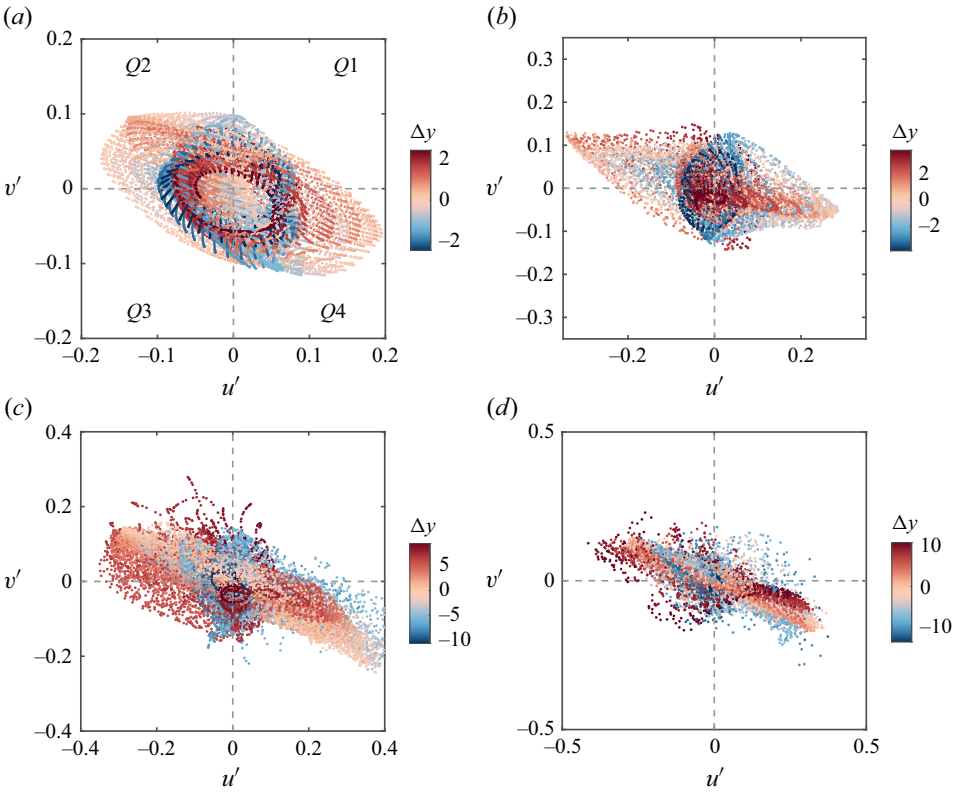


Figure 21. Scatter plots of velocity fluctuations u' and v' within minimum flow structure elements in different transition stages (regions): (*a*) $32.8 < x < 45.0$, $-2.5 < y < 2.5$, (*b*) $79.5 < x < 90.0$, $-4.0 < y < 4.0$, (*c*) $148.0 < x < 160.0$, $-12.0 < y < 8.0$, and (*d*) $242.0 < x < 253.0$, $-17.0 < y < 8.5$. The spanwise range of all four regions is $9.0 < z < 27.0$.

high-speed layer (red). In this stage (region), Λ-vortices appear and co-exist with 3-D waves. The quasi-streamwise vortices transport unmixed fluids from the upper high-speed layer downwards to the mixing centre through $Q4$ events, while they transport unmixed fluids from the low-speed layer upwards to the mixing centre through $Q1$ events. As the flow develops downstream, especially in regions with growing hairpin vortices (see figure 21*c*,*d*), the magnitude and occurrence frequency of ejection events increase in the upper layer, while sweep events become more prevalent in the lower layer. In those regions, the mixing layer develops into a turbulent state, with the hairpin vortices gradually breaking down into smaller-scale vortices.

5.3. *Split of the 3-D wave bulge*

In the vortex development stage (i.e. $x > 150$), the quasi-streamwise vortices are stretched and intensified, even with subsequent legs coalesced. This leads to the ejection of each leg at the flanks of the primary wave. The ejection caused by a Λ-vortex is stronger than the normal ejection induced by a 3-D wave, which results in the split of the 3-D wave bulge, marking the wave–vortex interaction; see figures 8(*d*) and 10(*d*).

It is noted that the interaction of oblique waves can indeed give rise to hairpin vortices, a phenomenon analysed by Sandham & Reynolds (1991), as we also observed in

https://doi.org/10.1017/jfm.2025.10548 Published online by Cambridge University Press

Case3. Kachanov (1994) had investigated the interaction of a plane Tollmien–Schlichting (T–S) wave (with a fundamental frequency) with a pair of oblique waves (with half the fundamental frequency). In their experiment, the T–S disturbance was introduced by a vibrating ribbon, while subharmonic oscillations were either excited by natural disturbances or amplified from priming oscillations. In present simulations, subharmonic oblique waves were directly introduced as a disturbance, which is consistent with the wave splitting phenomena.

Finally, it is beneficial to revisit the role of wave–vortex interaction in generation of Λ-vortices. In § 4.2, it has been demonstrated that the high-shear term $\partial\tilde{u}_x/\partial z$ out of local high strain rate S_{13} plays an important role in producing streamwise vorticity. This occurs at the interfacial region between low- and high-momentum zones, but with opposite shear directions. The appearance of high strain rate, as visualised on the material surface in figure 11(*b*), is consistent with this mechanism. Similarly, large $\partial\tilde{u}_y/\partial z$ out of S_{23} as displayed in figure 11(*c*) makes a significant contribution to the generation of $\tilde{\omega}_y$ at the early transition stage. Note that the formation of high S_{12} in figure 11(*a*) is the result of the wave motion because $\tilde{\omega}_y(\partial U_x/\partial y)$ never grows significantly until $\tilde{\omega}_y$ is strong enough.

6. Conclusions

The laminar-to-turbulent transition of a spatially developing mixing layer, which starts from the disturbance of a combination of a 2-D wave and a pair of 3-D oblique waves, is investigated by using DNS methods. The mechanism proposed by Lee & Wu (2008) regarding the generation of quasi-streamwise (Λ and hairpin) vortices in boundary layer flows is further examined for the mixing layer flow in the present study. Spatiotemporal evolutions of the material line and material surface are realised by tracking fluid particles in the computational process, as done in a previous study (Jiang *et al.* 2020*a*). It should be stressed that the initial location of a material line or a material surface may significantly affect its visualisation effect on the target flow pattern. Therefore, the initial positions of particles are designed such that the particles could eventually converge to the morphology of local flow structures.

A specific case with $M_c = 0.7$ is chosen in order to investigate the causal evolution of vortex structures from the 3-D wave structures. In consistency with previous research works, the co-existence state of wave and vortex structures is also observed in the early stage of mixing layer transition. Indeed, the 3-D wave mode (1, 1) proves to take the lead in kinetic energy growth during this stage. In combination with conditional statistics, the Lagrangian tracking method helps to reveal the dynamic co-evolution of wave and vortex structures as well as their interaction through the intermediary high strain rate structures. The conceptual model where 3-D perturbation waves give birth to Λ-vortices in the mixing layer is summarised as follows.

(i) First, evolutions of either timelines or material surfaces manifest that amplitudes of the wavy bulges gradually increase in both directions normal to the mixing layer. This increase in amplitude is consistent with the fluid lift-up or sweep-down events. Quadrant analysis suggests that the ejection/sweep events are generated on both sides of the centreline of the mixing layer.

(ii) Furthermore, the ejection/sweep motions surrounding the 3-D wave structures lead to the formation of local high strain rate layers, within which Λ-vortices are generated. At the peak of a 3-D wave, the shear $\partial u/\partial y$ along with lateral vortex stretching triggers the formation of a Λ-vortex head. At flanks of the 3-D wave, the magnitudes of S_{23}

https://doi.org/10.1017/jfm.2025.10548 Published online by Cambridge University Press

and S_{13} are relatively high due to the shear from ejection/sweep of fluids and spanwise gradient of u. The strain rate fields carried by the material surface show that higher S_{12} appear on the 'hillsides' of wave packets. Both S_{13} and S_{23} are observed to be concentrated in the wave-flank zones. The FTLE fields on the material surface also support that the fluid stretching is the most intense at the 'windward' and 'ridges' of the 3-D wave.

(iii) In addition, the shear parts of the high strain rate field ultimately give rise to quasi-streamwise legs of the Λ-vortices. Conditional statistics show that both the preferential alignment of the intermediate eigenvector of the strain rate tensor and the enstrophy are enhanced in high strain rate regions. The dominant contribution to the generation of streamwise vorticity comes from the stretching of streamwise fluctuating vorticity $\tilde{\omega}_x$ by mean shear $\partial U/\partial y$, and the tilting of mean spanwise vorticity Ω_z by spanwise fluctuating shear $\partial \tilde{u}_x/\partial z$.

(iv) Once the Λ-vortices are generated within the high shear layer with strong vorticity concentration, the tilting/stretching mechanism acts to deform them into hairpin-shaped structures, ultimately leading to their breakdown. This process is similar to what has been observed in boundary layer transition. It is inferred that the above process could be universal in any shear flows, but with discrepancies due to different boundary conditions, which remains to be further validated.

It might be beneficial to clarify that present results are obtained specifically for the case with $Mc = 0.7$, chosen to examine the causal development of vortex structures from 3-D wave formations. This value $Mc = 0.7$ represents a weakly compressible flow. As for lower Mach number conditions, Jiang *et al.* (2021) report a numerical study on the spatiotemporal wave-warping process in boundary layer flow at a very low Mach number (nearly incompressible), and claim a qualitatively similar mechanism for the formation and evolution of flow structures. In addition, the present simulation has also been extended to a case with $Mc = 1.4$. Similar wave–vortex interaction mechanisms are observed as expected, with the primary effect of the convective Mach number being the alteration of instability growth rates.

Overall, the present findings and conceptual model uncover the complex mechanism during the nonlinear stage of mixing layer transition. The underlying dynamics related to wave–vortex interactions in late-stage transition and fully developed turbulent mixing flow is open for further investigation.

Acknowledgements. The authors would like to thank Dr R. Wang for contributing the particle tracking code, and Professor C. Lee for insightful comments on this research work. J.C. is grateful to Professor W. Su, Professor Y. Zhao, Professor Z. She, Dr P. Chen, Dr A. Gao, Dr S. Zhang and C. Chen for many useful discussions. Numerical simulations were carried out on the Polars computing platform of Peking University in Beijing, China. Special thanks are addressed to X. Li for providing the single-phase fluid solver Opencfd-SC Ver 2.2b.

Funding. The authors acknowledge financial support provided by the National Natural Science Foundation of China under grant nos 92152202 and 12588201.

Declaration of interests. The authors report no conflict of interest.

Appendix A. Inflow disturbance

The basic flow profile of a mixing layer satisfies both the Rayleigh and Fjortoft criteria, thus is essentially unstable from the inviscid point of view. Small disturbances $\boldsymbol{u}'$ are usually superposed to the inflow stream $\boldsymbol{U}_\infty$ to reduce the development length for

https://doi.org/10.1017/jfm.2025.10548 Published online by Cambridge University Press

transition to turbulence in a finite computational domain. To study the mixing layer transition, two types of disturbances are usually applied at the inlet, i.e. artificial turbulence disturbances and eigenmode wave disturbances. Although the former is much closer to realistic applications, the latter is employed in the present study to investigate wave–wave interaction and the corresponding effect. Eigenmode waves from LST take the form

$$u_i' = \sum_n \mathring{A}_{i,n}\, \hat{\boldsymbol{\Phi}}_{i,n}(y)\, \exp[\mathrm{i}(\beta_n z - \omega_n t)], \tag{A1}$$

in which $\mathrm{i} = \sqrt{-1}$ is the imaginary unit, $\mathring{A}_{i,n}$ are the amplitudes of the nth eigenmode, and $\boldsymbol{\Phi}_{i,n}$, β_n and ω_n are the eigenfunctions, spanwise wavenumber and temporal frequency, respectively, from LST. Wave modes are denoted as (ω, β). In Case1, for example, the modes of a 2-D wave and a pair of oblique waves are selected for the normal velocity disturbance

$$v'(0, y, z, t) = a_0\, \phi_0(y)\, e^{-\mathrm{i}\omega_0 t} + a_1\, \phi_1(y)\, e^{\mathrm{i}(\beta_1 z - \omega_1 t)} + a_1\, \phi_1(y)\, e^{\mathrm{i}(-\beta_1 z - \omega_1 t)}, \tag{A2}$$

where $\omega_1 = 0.5\omega_0$, $a_m = \mathring{A}_{2,m}$ and $\phi_m = \Phi_{2,m}$, with $m = 0, 1$. This setting is similar to that in the numerical simulation from Sandham & Reynolds (1991), but in spatially developing form. The waves are initialised at a high amplitude in mode (1, 0), and in a low and equal amplitude in modes (0.5, 1) and (0.5, −1). Here, mode (ω_0, β) is selected as the reference mode. The above parameters are chosen such that the fundamental frequency and oblique wavenumber are the most unstable in LST.

Appendix B. Mean and disturbance vorticity

Substituting the double decomposition of velocity and vorticity (see (4.2)), along with decomposition of pressure and density $p = P + \tilde{p}$ and $\rho = \varrho + \tilde{\rho}$, into the vorticity equation (2.12), one can obtain the following equation for mean vorticity:

$$\begin{aligned}
\frac{\partial \boldsymbol{\Omega}}{\partial t} =& -(\boldsymbol{U}\cdot\nabla)\boldsymbol{\Omega} + (\boldsymbol{\Omega}\cdot\nabla)\boldsymbol{U} - \boldsymbol{\Omega}(\nabla\cdot\boldsymbol{U}) - \frac{1}{\varrho^2}\nabla P\cdot\nabla\varrho \\
&+ \frac{\mu}{Re}\left[\frac{1}{\varrho}\nabla^2\boldsymbol{\Omega} - \frac{1}{\varrho^2}\nabla\varrho\cdot\left(\nabla^2\boldsymbol{U} + \frac{1}{3}\nabla\left(\nabla\cdot\boldsymbol{U}\right)\right)\right] \\
&- \langle\tilde{\boldsymbol{u}}\cdot\nabla\tilde{\boldsymbol{\omega}}\rangle + \langle\tilde{\boldsymbol{\omega}}\cdot\nabla\tilde{\boldsymbol{u}}\rangle - \langle\tilde{\boldsymbol{\omega}}(\nabla\cdot\tilde{\boldsymbol{u}})\rangle - \frac{1}{\varrho^2}\langle\nabla\tilde{p}\cdot\nabla\tilde{\rho}\rangle \\
&- \frac{\mu}{Re}\frac{1}{\varrho^2}\left[\langle\nabla\tilde{\rho}\cdot\nabla^2\tilde{u}\rangle + \frac{1}{3}\left\langle\nabla\tilde{\rho}\cdot\nabla(\nabla\cdot\tilde{u})\right\rangle\right],
\end{aligned} \tag{B1}$$

where $\langle\cdot\rangle$ denotes the phase average, i.e. the ensemble average of all structures at the same evolutionary stage or phase. Subtracting (2.12) from (B1) yields the governing equation for fluctuating vorticity:

$$\begin{aligned}
\frac{\partial\tilde{\boldsymbol{\omega}}}{\partial t} =& -\tilde{\boldsymbol{u}}\cdot\nabla\boldsymbol{\Omega} - \boldsymbol{U}\cdot\nabla\tilde{\boldsymbol{\omega}} - (\tilde{\boldsymbol{u}}\cdot\nabla\tilde{\boldsymbol{\omega}} - \langle\tilde{\boldsymbol{u}}\cdot\nabla\tilde{\boldsymbol{\omega}}\rangle) \\
&- \boldsymbol{\Omega}(\nabla\cdot\tilde{\boldsymbol{u}}) - \tilde{\boldsymbol{\omega}}(\nabla\cdot\boldsymbol{U}) - [\tilde{\boldsymbol{\omega}}(\nabla\cdot\tilde{\boldsymbol{u}}) - \langle\tilde{\boldsymbol{\omega}}(\nabla\cdot\tilde{\boldsymbol{u}})\rangle] \\
&+ (\boldsymbol{\Omega}\cdot\nabla)\tilde{\boldsymbol{u}} + (\tilde{\boldsymbol{\omega}}\cdot\nabla)\boldsymbol{U} + (\tilde{\boldsymbol{\omega}}\cdot\nabla\tilde{\boldsymbol{u}} - \langle\tilde{\boldsymbol{\omega}}\cdot\nabla\tilde{\boldsymbol{u}}\rangle)
\end{aligned}$$

https://doi.org/10.1017/jfm.2025.10548 Published online by Cambridge University Press

$$
\begin{aligned}
&+\frac{1}{\varrho^2}[\nabla P\cdot\nabla\tilde{\rho}+\nabla\tilde{p}\cdot\nabla\varrho+(\nabla\tilde{p}\cdot\nabla\tilde{\rho}-\langle\nabla\tilde{p}\cdot\nabla\tilde{\rho}\rangle)]\\
&+\frac{\mu}{Re}\frac{1}{\varrho}\nabla^2\tilde{\boldsymbol{\omega}}-\frac{\mu}{Re}\frac{1}{\varrho^2}\nabla\varrho\cdot\left[\nabla^2\tilde{\boldsymbol{u}}+\frac{1}{3}\nabla(\nabla\cdot\tilde{\boldsymbol{u}})\right]\\
&-\frac{\mu}{Re}\frac{1}{\varrho^2}\nabla\tilde{\rho}\cdot\left[\nabla^2\boldsymbol{U}+\frac{1}{3}\nabla(\nabla\cdot\boldsymbol{U})\right]\\
&-\frac{\mu}{Re}\frac{1}{\varrho^2}(\nabla\tilde{\rho}\cdot\nabla^2\tilde{\boldsymbol{u}}-\langle\nabla\tilde{\rho}\cdot\nabla^2\tilde{\boldsymbol{u}}\rangle)\\
&-\frac{\mu}{Re}\frac{1}{\varrho^2}\frac{1}{3}(\nabla\tilde{\rho}\cdot\nabla(\nabla\cdot\tilde{\boldsymbol{u}})-\langle\nabla\tilde{\rho}\cdot\nabla(\nabla\cdot\tilde{\boldsymbol{u}})\rangle).
\end{aligned}
\tag{B2}
$$

The physical meanings of the terms on the right-hand side of (B2) are interpreted as follows. Linear terms include the vortex filament's induction $\tilde{\boldsymbol{u}}\cdot\nabla\boldsymbol{\Omega}$, the advection by mean flow $\boldsymbol{U}\cdot\nabla\tilde{\boldsymbol{\omega}}$, the dilatation effects due to compressibility $\boldsymbol{\Omega}(\nabla\cdot\tilde{\boldsymbol{u}})$ and $\tilde{\boldsymbol{\omega}}(\nabla\cdot\boldsymbol{U})$, the mean vortex stretching by fluctuating strain rate $(\boldsymbol{\Omega}\cdot\nabla)\tilde{\boldsymbol{u}}$, the fluctuating vortex stretching by mean strain rate $(\tilde{\boldsymbol{\omega}}\cdot\nabla)\boldsymbol{U}$, and the baroclinic effects because of compressibility $\nabla P\cdot\nabla\tilde{\rho}$ and $\nabla\tilde{p}\cdot\nabla\varrho$. The other terms are contributions from either nonlinearity or viscosity.

References

Adrian, R.J. 2007 Hairpin vortex organization in wall turbulence. *Phys. Fluids* **19** (4), 041301.

Ashurst, W.T., Kerstein, A.R., Kerr, R.M. & Gibson, C.H. 1987 Alignment of vorticity and scalar gradient with strain rate in simulated Navier–Stokes turbulence. *Phys. Fluids* **30** (8), 2343–2353.

Bechlars, P. & Sandberg, R.D. 2017 Variation of enstrophy production and strain rotation relation in a turbulent boundary layer. *J. Fluid Mech.* **812**, 321–348.

Benney, D.J. 1961 A non-linear theory for oscillations in a parallel flow. *J. Fluid Mech.* **10** (2), 209–236.

Chen, J.H., Cantwell, B.J. & Mansour, N.N. 1989 The topology and vorticity dynamics of a three-dimensional plane compressible wake. In *Tenth Australasian Fluid Mechanics Conference*. University of Melbourne.

Croswell, J.W. 1985 On the energetics of primary and secondary instabilities in plane Poiseuille flow. *PhD thesis*, Virginia Polytechnic Institute and State University.

Green, M.A., Rowley, C.W. & Haller, G. 2007 Detection of Lagrangian coherent structures in three-dimensional turbulence. *J. Fluid Mech.* **572**, 111–120.

Grosch, C.E. & Jackson, T.L. 1991 Inviscid spatial stability of a three-dimensional compressible mixing layer. *J. Fluid Mech.* **231**, 35–50.

Haidari, A.H. & Smith, C.R. 1994 The generation and regeneration of single hairpin vortices. *J. Fluid Mech.* **277**, 135–162.

Haller, G. 2001 Distinguished material surfaces and coherent structures in three-dimensional fluid flows. *Phys. D: Nonlinear Phenomena* **149** (4), 248–277.

Hama, F.R., Long, J.D. & Hegarty, J.C. 1957 On transition from laminar to turbulent flow. *J. Appl. Phys.* **28** (4), 388–394.

Head, M.R. & Bandyopadhyay, P. 1981 New aspects of turbulent boundary-layer structure. *J. Fluid Mech.* **107**, 297–338.

Herbert, T. 1988 Secondary instability of boundary layers. *Annu. Rev. Fluid Mech.* **20** (1), 487–526.

Jang, P.S., Benney, D.J. & Gran, R.L. 1986 On the origin of streamwise vortices in a turbulent boundary layer. *J. Fluid Mech.* **169**, 109–123.

Jiang, X.Y., Atoufi, A., Zhu, L., Lefauve, A., Taylor, J.R., Dalziel, S.B. & Linden, P.F. 2023 Geometry of stratified turbulent mixing: local alignment of the density gradient with rotation, shear and viscous dissipation. *J. Fluid Mech.* **977**, R5.

Jiang, X.Y., Gu, D.W., Lee, C.B., Smith, C.R. & Linden, P.F. 2021 A metamorphosis of three-dimensional wave structure in transitional and turbulent boundary layers. *J. Fluid Mech.* **914**, A4.

Jiang, X.Y., Lee, C.B., Chen, X., Smith, C.R. & Linden, P.F. 2020*a* Structure evolution at early stage of boundary-layer transition: simulation and experiment. *J. Fluid Mech.* **890**, A11.

https://doi.org/10.1017/jfm.2025.10548 Published online by Cambridge University Press

JIANG, X.Y., LEE, C.B., SMITH, C.R., CHEN, J.W. & LINDEN, P.F. 2020*b* Experimental study on low-speed streaks in a turbulent boundary layer at low Reynolds number. *J. Fluid Mech.* **903**, A6.
JIANG, X.Y., LEFAUVE, A., DALZIEL, S.B. & LINDEN, P.F. 2022 The evolution of coherent vortical structures in increasingly turbulent stratified shear layers. *J. Fluid Mech.* **947**, A30.
JIMÉNEZ, J. 2018 Coherent structures in wall-bounded turbulence. *J. Fluid Mech.* **842**, P1.
KACHANOV, Y.S. 1994 Physical mechanisms of laminar–boundary-layer transition. *Annu. Rev. Fluid Mech.* **26** (1), 411–482.
KIDA, S. & TANAKA, M. 1994 Dynamics of vortical structures in a homogeneous shear flow. *J. Fluid Mech.* **274**, 43–68.
KIM, J., MOIN, P. & MOSER, R. 1987 Turbulence statistics in fully developed channel flow at low Reynolds number. *J. Fluid Mech.* **177**, 133–166.
KLEIN, M., SADIKI, A. & JANICKA, J. 2003 A digital filter based generation of inflow data for spatially developing direct numerical or large eddy simulations. *J. Comput. Phys.* **186** (2), 652–665.
KONRAD, J.H. 1976 An experimental investigation of mixing in two-dimensional turbulent shear flows with applications to diffusion-limited chemical reactions. *NASA STI/Recon Tech. Rep. No.* **77**, 28462.
LANDAU, L.D. & LIFSHITZ, E.M. 2013 *Fluid Mechanics* (2nd edn, Course of Theoretical Physics, vol. 6, ed. L. P. Pitaevskii). Butterworth-Heinemann/Elsevier.
LAWSON, J.M. & DAWSON, J.R. 2015 On velocity gradient dynamics and turbulent structure. *J. Fluid Mech.* **780**, 60–98.
LEE, C.B. 1998 New features of CS solitons and the formation of vortices. *Phys. Lett. A.* **247** (6), 397–402.
LEE, C.B. 2000 Possible universal transitional scenario in a flat plate boundary layer: measurement and visualization. *Phys. Rev. E* **62** (3), 3659–3670.
LEE, C.B. & WU, J.Z. 2008 Transition in wall-bounded flows. *Appl. Mech. Rev.* **61** (3), 030802.
LI, D., PEYVAN, A., GHIASI, Z., KOMPERDA, J. & MASHAYEK, F. 2021 Compressibility effects on energy exchange mechanisms in a spatially developing plane free shear layer. *J. Fluid Mech.* **910**, A9.
MCKEON, B.J. 2017 The engine behind (wall) turbulence: perspectives on scale interactions. *J. Fluid Mech.* **817**, P1.
MOIN, P., LEONARD, A. & KIM, J. 1986 Evolution of a curved vortex filament into a vortex ring. *Phys. Fluids* **29** (4), 955–963.
PERRY, A.E. & CHONG, M.S. 1982 On the mechanism of wall turbulence. *J. Fluid Mech.* **119**, 173–217.
PERRY, A.E. & MARUSIC, I. 1995 A wall-wake model for the turbulence structure of boundary layers. Part 1. Extension of the attached eddy hypothesis. *J. Fluid Mech.* **298**, 361–388.
REYNOLDS, O. 1883 An experimental investigation of the circumstances which determine whether the motion of water shall be direct or sinuous, and of the law of resistance in parallel channels. *Phil. Trans. R. Soc. Lond.* **174**, 935–982.
RIST, U. & FASEL, H. 1995 Direct numerical simulation of controlled transition in a flat-plate boundary layer. *J. Fluid Mech.* **298**, 211–248.
ROBINSON, S.K. 1991 Coherent motions in the turbulent boundary layer. *Annu. Rev. Fluid Mech.* **23** (1), 601–639.
SANDHAM, N.D. 1989 A numerical investigation of the compressible mixing layer. PhD thesis, Stanford University.
SANDHAM, N.D. & REYNOLDS, W.C. 1991 Three-dimensional simulations of large eddies in the compressible mixing layer. *J. Fluid Mech.* **224**, 133–158.
SANDHAM, N.D. & YEE, H.C. 1989 A numerical study of a class of TVD schemes for compressible mixing layers, *Tech. Rep.* NASA-TM-102194, NASA Ames Research Center.
SHU, C.W. 1998 *Essentially Non-oscillatory and Weighted Essentially Non-oscillatory Schemes for Hyperbolic Conservation Laws*. Springer.
SMITH, C.R., WALKER, J.D.A., HAIDARI, A.H. & SOBRUN, U. 1991 On the dynamics of near-wall turbulence. *Phil. Trans. R. Soc. Lond. A* **336** (1641), 131–175.
TOWNSEND, A.A. 1999 *The Structure of Turbulent Shear Flow*, 2nd edn. Cambridge University Press.
WALEFFE, F. 1997 On a self-sustaining process in shear flows. *Phys. Fluids* **9** (4), 883–900.
WU, X.H. & MOIN, P. 2009 Direct numerical simulation of turbulence in a nominally zero-pressure-gradient flat-plate boundary layer. *J. Fluid Mech.* **630**, 5–41.
ZHAO, Y.M., YANG, Y. & CHEN, S.Y. 2016 Evolution of material surfaces in the temporal transition in channel flow. *J. Fluid Mech.* **793**, 840–876.
ZHOU, J., ADRIAN, R.J., BALACHANDAR, S. & KENDALL, T.M. 1999 Mechanisms for generating coherent packets of hairpin vortices in channel flow. *J. Fluid Mech.* **387**, 353–396.
ZHOU, Q., HE, F. & SHEN, M.Y. 2012 Direct numerical simulation of a spatially developing compressible plane mixing layer: flow structures and mean flow properties. *J. Fluid Mech.* **711**, 437–468.

https://doi.org/10.1017/jfm.2025.10548 Published online by Cambridge University Press